Coupled micro-faulting and pressure solution creep overprinted on quartz schist deformed by intracrystalline plasticity during exhumation of the Sambagawa metamorphic rocks, southwest Japan

Toru Takeshita[a,*] and Abdel-Hamid El-Fakharani[b]

[a]*Department of Natural History Sciences, Graduate School of Science, Hokkaido University, Sapporo 060-0810, Japan*

[b]*Department of Structural Geology and Remote Sensing, Faculties of Earth Sciences, King Abdulaziz University, Jeddah 21589, Saudi Arabia*

[*] Corresponding author. Tel.: +81 117064636; fax: +81 117460394

E-mail address: torutake@mail.sci.hokudai.ac.jp (T. Takeshita)

Abstract

In the Sambagawa schist, southwest Japan, while ductile deformation pervasively occurred at D_1 phase during exhumation, low-angle normal faulting was locally intensive at D_2 phase under the conditions of frictional-viscous transition of quartz (*c.* 300 ^{o}C) during further exhumation into the upper crustal level. Accordingly, the formation of D_2 shear bands was overprinted on type I crossed girdle quartz *c*-axis fabrics and microstructures formed by intracrystalline plasticity at D_1 phase in some quartz schists. The quartz *c*-axis fabrics became weak and finally random with increasing shear, accompanied by the decreasing degree of undulation of recrystallized quartz grain boundaries, which resulted from the increasing portion of straight grain boundaries coinciding with the interfaces between newly precipitated quartz and mica. We interpreted these facts as caused by increasing activity of pressure solution: the quartz grains were dissolved mostly at platy quartz-mica interface, and precipitated with random orientation and pinned by mica, thus having led to the obliteration of existing quartz *c*-axis fabrics. In the sheared quartz schist, the strength became reduced by the enhanced pressure solution creep not only due to the reduction of diffusion path length caused by increasing number of shear bands, but also to enhanced dissolution at the interphase boundaries.

Keywords: Pressure solution; Shear bands; Obliteration of quartz *c*-axis fabrics; Pinning structure

1. Introduction

Rheology in rocks is important to understand dynamics in the earth. The rheology in the upper crust has been modeled with the brittle upper part deforming by frictional faulting, and ductile lower part rate-controlled by power-law creep in quartz or feldspar (e.g. Kohlsted et al., 1995). Such modeling of upper crustal rheology seems to be relevant, because it can predict the lower-limit depth of hypocenters of inland earthquakes based on the depth of frictional-viscous transition (e.g. Stewart et al., 2000), which is consistent with the naturally observed depth of 15-20 km in mobile belts (e.g. Duebendorfer et al., 1998). On the other hand, this strength profile has been criticized, because such high differential stresses, say a few hundreds of megapascal at the depth of seismogenic zones, have been never reported from natural fault zones, e. g. the San Andreas Fault zone, where a differential stress of 20 MPa is inferred from heat flow data (Lachenbruch and Sass, 1992). Another question on the strong upper crust comes from the modeling of exhumation of metamorphic rocks. Beaumont et al. (2004) conducted numerical modeling of channel flows for the Himalayan metamorphic rocks, and showed that channeling midcrustal rocks (i.e. metamorphic rocks) are never able to be extruded along brittle faults in the upper crust, unless the coefficient of internal friction is much less than the experimental ones, say by one-third. The fact suggests that the coefficient of internal friction on

natural faults was indeed decreased by some softening mechanisms during exhumation of metamorphic rocks.

In natural deformation, in particular at frictional-viscous transition conditions, we know that both micro-faulting shown by formation of shear bands along which mica was precipitated (e.g. Schrank et al., 2008), and pressure solution creep (e.g. Hippertt, 1994; Takeshita and Hara, 1998, Stöckhert, 2002) are important deformation mechanisms. In fact, Bos and Spiers (2002) and Niemeijer and Spiers (2005) theoretically showed that at most of the depth range (ca. 5-20 km) in the upper part of the crust, frictional sliding in mica accommodated by pressure solution of quartz controls the rheology, the strength of which is less than one third of that predicted by the Byerlee (1978)'s law. However, as Bos and Spiers (2002) admitted, the numerical modeling of frictional-viscous deformation is still in infancy, because material constants, in particular, grain boundary friction and diffusion coefficients at high pressure conditions, which greatly affect the final results, are still uncertain. Furthermore, some predictions on pressure solution creep in quartz give an unrealistically high rate of pressure-solution creep, c. $10^{-7 \text{ to } -11}$/s at T=350 ^{o}C and σ=100 MPa compared to natural ones, also because diffusion coefficients at high pressure conditions are not well constrained (Nakashima, 1995; Shimizu, 1995). Therefore, considering the limitation of numerical modeling at current stages, natural observation of pressure solution creep of quartzite is important to

constrain its flow law.

In this paper, we describe the penetrative development of both deformation microstructures in quartz schist samples from the Sambagawa metamorphic rocks, southwest Japan: micro-faults (i.e. shear bands) indicative of frictional sliding, and grain microstructures and quartz *c*-axis fabrics indicative of pervasive pressure solution creep. These microstructures were formed during the final exhumation into upper crustal levels at the frictional-viscous transition conditions, which was called D_2 phase in the previous studies (Osozawa and Publis, 2007; El-Fakharani and Takeshita, 2008). Then, we will interpret how the microstructures were developed with increasing strain (i.e. deformation histories). Based on these observations and interpretations, we will discuss a model of large strain deformation, and the possible large degree of strain softening due to frictional sliding accommodated by pressure solution creep in quartz-mica aggregates deformed at frictional-viscous transition regions.

2. Geological setting

The Sambagawa belt is a high-*P/T* type metamorphic belt that extends from eastern Kyushu to the Kanto mountains, north-west of Tokyo, over 700-800 km, throughout south-west Japan (Fig. 1a).

It is widely exposed in central Shikoku, where the maximum width is ca. 30 km. To the north this belt is separated from the low-*P/T* type Ryoke metamorphic belt by the Median Tectonic Line (MTL). Miyashiro (1961) originally suggested that the low- and high-*P/T* type paired Ryoke and Sambagawa metamorphic belts were formed under a volcanic arc and at a subduction zone, respectively with a 100-200 km separation distance. However, recent studies have suggested that they originated from an accretionary prism at places far from each other along a common subduction zone to the Pacific Ocean, which were later juxtaposed as a result of Cretaceous left-lateral transcurrent faulting along the MTL oblique to the arc (Taira et al., 1989; Brown, 1998; Sakashima et al., 2003).

The Sambagawa metamorphic rocks are inferred to have originated from Jurassic accretionary complexes based on radiolarian fossils (e.g. Isozaki and Itaya, 1990; Faure et al., 1991), which consist of pelitic, psammitic, mafic and quartz schists with rare serpentinite and metagabbro. Okamoto et al. (2004) have reported SHRIMP U-Pb zircon ages, varying between 132 and 112 Ma for quartz-bearing eclogites, which are interpreted as the age of peak-metamorphism. Amphibole and phengite yielded K-Ar (or ^{40}Ar / ^{39}Ar) ages ranging from 94 to 65 Ma (e.g. Itaya and Takasugi 1988; Takasu and Dallmeyer 1990), probably indicating the ages of exhumation.

Based on the appearance of index minerals in pelitic schists, the Sambagawa metamorphic

rocks can be divided into four zones (Fig. 1b), starting with the lowest metamorphic grade: chlorite zone (300-360 ºC, 5.5-6.5 kbar), garnet zone (440±15 ºC, 7-8.5 kbar), albite-biotite zone (520±25 ºC, 8-9.5 kbar), and oligoclase-biotite zone (610±20 ºC, 10-11 kbar), respectively (e.g. Higashino, 1990; Enami et al., 1994). The metamorphic zonal sequence is inverted in the lower structural level from the chlorite to oligoclase-biotite zone, while it is normal in the upper structural level from the albite-biotite to garnet zone (Fig. 1c). This structure has been interpreted either as a large-scale recumbent fold (Banno et al., 1978; Wallis et al., 1992) or as thrust sheets (Hara et al., 1977; Faure, 1985; Higashino, 1990) formed after the peak metamorphism.

Based on field observations and structural studies, we can conclude that deformation structures of Sambagawa metamorphic belt were formed at three distinct deformation phases (D_1, D_2 and D_3) under retrograde conditions during the exhumation stages (e.g. Hara et al., 1977; Faure, 1983; Wallis, 1990). The D_1 phase is characterized by ductile flow in an east-west direction, and during this phase of deformation the main foliation and lineation were formed. The lineation is defined by the shape-preferred orientation (SPO) of matrix amphiboles, which grew under retrograde conditions (Hara et al., 1990, 1992; Wallis et al., 1992; Nakamura and Enami, 1994; Wintsch et al., 1999; Banno, 2000; Yagi and Takeshita, 2002; Okamoto and Toriumi, 2004, 2005), and by elongated quartz (Takeshita and Yagi, 2004), whereas the shape-preferred orientation of phengite and flattened quartz

define the foliation.

D_2 phase in the chlorite zone is characterized by south-vergent overturned folds with crenulation cleavages (Hara et al., 1977; Faure, 1983). On the other hand, the D_2 folds in the high grade zones are characterized by recumbent folds (e.g. Wallis, 1990). Both Osozawa and Pavlis (2007) and El-Fakharani and Takeshita (2008) have recently reported dominant activity of D_2 low-angle north-dipping normal faults in the high grade zones, which accompany north-vergent recumbent folds.

D_3 folds are open upright folds with E-W to WNW-ESE trending horizontal axes. The D_3 folds are interpreted to have been formed after exhumation (Banno and Sakai, 1989), in relation to left-lateral displacement along MTL (Hara et al., 1977; Shiota et al., 1993).

3. Post-D_1 deformations in the Niihama area and sample localities

The Sambagawa metamorphic rocks in the Niihama area mostly belong to the albite-biotite zone of the upper structural level, while some of them belong to the oligoclase-biotite and garnet zones (Higashino, 1990, Fig. 1). The map-scale distribution of the Sambagawa metamorphic rocks in central Shikoku are mostly controlled by the major D_3 folds. In the Asemi river-Kamio river section

(I-I' section in Fig. 1), the Yakushi antiform to the north and Tsuneyama synform to the south are easily identified, where these metamorphic rocks strike E-W to NW-SE and dip either N or S. These map-scale D_3 folds could be extended from the Asemi and Kamio river areas to the Niihama area in the WNW direction with decreasing the layer thickness, as mentioned below.

In the Niihama area, the thickness of the whole metamorphic sequence from the chlorite zone in the lower structural level to the garnet zone in the upper structural level is much thinner than that in the Asemi river area, based on the exposed width 5 km versus 10 km in each area, respectively. This fact could be attributed to the difference in the displacement of late-stage $\boldsymbol{D_2}$ normal faulting at both areas. In fact, in the Niihama area the rocks are much more severely faulted than in the Asemi river area, and Hara et al. (1992) called the zone between the MTL and the upper boundary of the thick mafic schist distributed in the SE corner of the study area (Fig. 2) the Ojoin mélange zone. Both Fukunari and Wallis (2007) and El-Fakharani and Takeshita (2008) analyzed the fault systems in this area, and concluded that most of these are low-angle normal faults dipping NNW, which can be correlated with those in the Asemi river area (Takeshita and Yagi, 2004). Although the metamorphic layers (D_1 foliation) are clearly cut by these normal faults, these are significantly dragged, indicating the semi-brittle nature of the faulting (Fig. 3a). In addition, the fault plane is often coated by the quartz slickenfibre dominantly showing a top-to-the-NNW-sense of shear (Fukunari and Wallis,

2007; El-Fakharani and Takeshita, 2008, Fig. 3b).

Analyzed quartz schist samples are collected from 5 localities from the garnet zone of the upper structural level (Higashino, 1990) along the upper stream of Nishinotani river (Fig. 2), where a few thick quartz schist layers up to c. 100 m thick are exposed. Although the short wavelength D_3 folds are present in this area, the foliation mostly strikes east-west and dips north at moderate to high angles (Fig. 2), and the lineation trends east-west and dips horizontally. These samples are named as Nishi-1, -2, -3, -4 and -5, respectively, among which samples Nishi-1, -2 and -3 were collected from localities in close proximity to each other.

For each sample, one thin section was made, which is cut normal to the foliation and parallel to the lineation (i.e. *XZ* section). Here, the *X*- and *Z*-axes denote the directions parallel to the lineation, and normal to the foliation, respectively. For these thin sections from each sample, microstructures in one or two domains were analyzed, which were named by capital alphabetical letters (e.g. Nishi-5-A). Further, just for the purpose of analyzing an appropriate number of quartz grains with the image analysis software, the domains were further divided into subdomains, which were termed by numbers (e.g. Nishi-5-A-1, Table 1).

4. Methods to analyze microstructures in quartz grains and area fraction of mica grains:

U-stage measurements and image analyses

In this research, not only the *c*-axis fabrics and microstructures of recrystallized quartz grains, but also the area fraction of phengite (referred to as mica hereafter) in deformed quartz schist samples have been analyzed. While quartz *c*-axis orientations of *c.* 200 grains were measured for each domain with a universal stage (U-stage) mounted on a petrographic microscope, the microstructural analyses were conducted by the Image analyses of microphotographs of the *XZ* thin sections using a free software NIH (National Institute of Health, 1999) Image (now called ImageJ). Furthermore, microstructural analyses were also conducted with a transmission electron microscope (TEM) at an accelerating voltage of 200 kV installed at Hokkaido University for representative recrystallized quartz grains.

For recrystallized quartz grains, we have first manually traced the grain boundaries on microphotographs of the *XZ* thin sections under crossed polarizers with λ-plate inserted at the magnifications of 100 times, which has been conducted with the Adobe Photoshop software (Fig. 4). Here, we refer to three images at the orientations rotated by $\pm 30^{o}$ about the microscope axis from the reference orientation to draw the grain boundaries. We adopt this procedure, because the large changes of interference colors of quartz grains, which are caused by small amount of rotation about

the microscope axis under crossed polarizers (i.e. extinction at every 90^o rotation), make the fairly different images of grain boundaries at the three orientations. Hence, more accurate determination of the grain boundaries can be possible, referring to these three images. Here, we only traced grain boundaries, but not subgrain boundaries across which grains are misoriented by angles less than *c.* 10^o. The traced boundary lines are then processed with the NIH Image software. Using this software, all the grains enclosed by the traced boundaries are sequentially numbered, and the area (*S*) and perimeter (*P*) of each grain are calculated. Also, the lengths of long (*a*) and short (*b*) axes of a best-fit ellipse, and the orientation of long axis (i.e. angle ϕ) relative to the reference orientation are calculated for each grain using the software.

From the microstructural data for each recrystallized quartz grain obtained with the NIH Image, we calculated the following values and constructed various diagrams. First, the size of each recrystallized grain is defined as the diameter of equivalent circle (i.e. circle with the same area as that of each recrystallized grain) D_{eq}, which is calculated from the area (*S*) of each recrystallized grain, as follows.

$$D_{eq} = 2\sqrt{\frac{S}{\pi}} \qquad (1)$$

The average size ($\overline{D_{eq}}$) over all the recrystallized quartz grains in each subdomain from the quartz schist samples is then computed (Table 1). The aspect ratio, *R* of each recrystallized grain is

calculated as follows.

$$R = {}^{a}/_{b} \qquad (2)$$

Subsequently, the average aspect ratio ($\bar{R}$) over all the recrystallized quartz grains in each subdomain from the quartz schist samples was then computed (Table 1). Further, the R/ϕ diagram, which is useful to show the shape preferred orientation (SPO) of elongated grains (e.g. Ghosh, 1993), was constructed. Here, ϕ is the angle between the trace of foliation and the long axis of each recrystallized grain determined with the NIH Image on the *XZ*-section, and defined as positive and negative for west and east dipping grains, respectively.

In this paper, in order to assess the degree of undulation of boundaries of recrystallized quartz grains with different sizes, the average normalized perimeter ($\overline{P_{nor}} = {}^{\bar{P}}/_{\overline{P_{eq}}}$) was calculated (Fig. 5, Table 1). Here, $\bar{P}$ and $\overline{P_{eq}}$ are the average perimeters of real and equivalent (i.e. fitted) ellipses over all the grains, respectively, and the perimeter of a fitted ellipse for individual grains (P_{eq}) is calculated using the following Eq. (3).

$$P_{eq} = 2\pi\sqrt{\frac{\left(\left(\frac{a}{2}\right)^2+\left(\frac{b}{2}\right)^2\right)}{2}} \qquad (3)$$

In this research, the area fraction of mica has been also determined for the same domains where quartz microstructures and *c*-axis fabrics were analyzed. For the determination of area fraction of mica, the grain boundaries of mica have been again manually traced with the Adobe Photoshop

software (Fig. 4), and the area of each grain enclosed by the traced grain boundaries has been calculated with the NIH Image on the microphotographs of *XZ*-sections from the quartz schist samples. Subsequently, the area fraction of mica relative to the total area on the *XZ*-section has been calculated for each domain. Note that the calculated 2-D area fraction of mica could be significantly different from the true 3-D volume fraction of mica, because the value does not take into account the effect of platy shape of mica on the volume fraction.

5. Results: microstructural analyses of quartz schist samples deformed at D_2 phase

5.1. Microstructures of analyzed quartz schist samples deformed at D_2 phase

The microstructures in analyzed samples except for Nishi-5 are characterized by lenses consisting of relict coarse recrystallized quartz grains surrounded by shear bands or micro-shear zones. Relict recrystallized quartz grains in the quartz lenses have ellipsoidal shape with lobate boundaries and often show wavy extinction and kink bands (Fig. 6a), which are formed at D_1 phase and essentially similar to microstructures of recrystallized quartz grains in quartz schist from the other localities of Sambagawa metamorphic rocks (e.g. Toriumi et al., 1986; Tagami and Takeshita,

1998; Yagi and Takeshita, 2002).

In all the analyzed samples, shear bands were pervasively developed at D_2 phase, although the degree of development is different among the samples. Shear bands were initially developed as narrow bands decorated by newly grown aligned mica (Fig. 6b), which were sometimes developed as conjugate sets. It is noted that not only the long axes of recrystallized quartz grains were bent towards the orientation of shear bands by dragging, forming deformation bands, but also very-fine quartz grains were formed along shear bands (Fig. 6b). Very-fine-grained quartz aggregates along narrow shear bands originated as dynamically recrystallized quartz, because these are formed in highly strained quartz along shear bands (Fig. 6c). Shear bands became wide and often developed to the ones with the widths up to 1 mm with increasing amount of shear (i.e. micro-shear zones), which consist of aggregates of very-fine-grained quartz on the order of 1-10 μm and aligned mica (Figs. 6d, e, f). Chlorite is also developed in these sheared samples, not along shear bands, but in some dilatant space (Figs. 6f, g). Also, it should be noted that dissolution of quartz was extensive at the interface between quartz lens and micro-shear zone, where the recrystallized quartz grains were perhaps truncated by platy mica grains indicating dissolution front (Fig. 6e, cf. Hippertt, 1994).

In samples Nishi-1 and Nishi-4, shear bands are least developed and micro-shear zones are little developed, whereas in samples Nishi-2 and Nishi-3, shear bands are most developed and

micro-shear zones are abundant, which occupy the area fraction as much as 50% (i.e. lens-matrix microstructure, Figs. 6d, e). In sample Nishi-5, although micro-shear zones are developed, their densities are much lower than those in Nishi-2 and Nishi-3 (Figs. 6f, g). Rather, this quartz schist sample mostly consists of relatively coarse quartz grains showing irregular shape with more straight boundaries, where the volume fraction of mica is significantly high (Figs. 6f, g). Straight grain boundaries are formed by pinning of grain boundaries of quartz on mica. Also, in these quartz grains, wavy extinction is very weak.

For microstructural analyses, in Nishi-1 and Nishi-4 with dominant relict recrystallized grain microstructures, a domain which includes few shear bands has been arbitrarily chosen (Table 1). For Nishi-5, two domains which do not include micro-shear zones have been also arbitrarily chosen. For samples Nishi-2 and Nishi-3 with high area fractions of shear bands and micro-shear zones, shear bands are also developed in the quartz lenses to various degrees. For these samples, we have separately chosen one domain of quartz lens with relict microstructures relatively preserved, and one significantly sheared, which are named for example Nishi-2-R and Nishi-2-S, respectively. Here, “R” and “S” stand for “relict” and “sheared”, respectively. Not only the area fraction of mica which is mostly aligned along shear bands is higher (Table 1), but also the degree of wavy extinction in quartz grains is weaker in the latter than the former domain. The differences in grain microstructure

between different domains from different samples have been quantitatively analyzed with the NIH Image analysis, as explained in the method section.

In this research, microstructural analyses were also conducted with a TEM for recrystallized quartz grains from a relict domain of sample Nishi-1 and a sheared domain of sample Nishi-2 (Nishi-2-S). Although in recrystallized quartz grains from both domains, dislocations are present, dislocation substructures are much different between the two domains (Fig. 7). First, free dislocation densities are significantly higher in recrystallized quartz grains from Nishi-1 (4.7-6.5$\times 10^8$ /cm^2, n=6) than Nishi-2-S (2.1-3.0$\times 10^8$/cm^2, n=4), where n is the number of analyzed microdomains (Fig. 7). Second, tangled dislocations are common in recrystallized quartz grains from Nishi-1, while such dislocations are absent in those from Nishi-2-S. Third, while sub-boundaries defined by arrays or networks of dislocations are abundant in recrystallized quartz grains from Nishi-1, such substructures are absent in those from Nishi-2-S.

5.2. Quartz c-axis fabric

Quartz *c*-axis fabrics have been shown in equal-area and lower-hemisphere projections for domains from all the quartz schist samples (Fig. 8). It is clear from these figures that quartz *c*-axis

fabrics in some domains in the analyzed quartz schist samples (Nishi-1-A, Nishi-2-R, Nishi-3-R, and Nishi-4-A in Fig. 8a) show a strong type I (Lister, 1977) crossed girdle pattern with monoclinic symmetry (i.e. 180^o rotation symmetry about the *Y*-axis parallel to the foliation and normal to the lineation). On the other hand, that in domains Nishi-5-A, B is random (Fig. 8c). The quartz *c*-axis fabrics in the sheared domains (e.g. Nishi-2-S, Nishi-3-S) are weaker than those in the domains of the first group, but their skeleton of type I crossed girdle pattern and monoclinic symmetry indicating shear deformation are still discerned (Fig. 8b).

We have calculated the fabric intensity (Lisle, 1985) for each *c*-axis fabric from the normalized eigenvalues (S_1, S_2 and S_3) of orientation tensors (Woodcock, 1977) determined with the Stereonet program by Allmendinger (1988), which is shown in Table 1 and next to each *c*-axis fabric diagram (Fig. 8). The fabric intensity *FI* is defined as follows,

$$FI = \frac{15}{2}\sum_{i=1}^{3}(S_i - \frac{1}{3})^2 \qquad (5)$$

Based on the values of fabric intensity (*FI*), the strong, weak and random quartz *c*-axis fabrics are defined as those with $FI \geq 0.45$, $0.2 \leq FI < 0.45$ and $FI < 0.2$, respectively (Fig. 8).

In each of the asymmetric quartz *c*-axis fabrics (i.e. strong and weak fabrics with monoclinic symmetry), the leading and trailing edges of fabric skeleton (Law, 1987) can be determined (inset diagram of Fig. 8). The disposition of these edges all indicates shear deformation with a

top-to-the-west sense, same as that commonly observed in quartz schist samples from other localities in the Sambagawa metamorphic rocks of central Shikoku (e.g. Wallis et al., 1992; Yagi and Takeshita, 2002; Takeshita and Yagi, 2004).

5.3. Results of image analyses of microstructures in recrystallized quartz grains

The average equivalent diameter ($\overline{D_{eq}}$), perimeter ($\bar{P}$), aspect ratio ($\bar{R}$), equivalent perimeter ($\overline{P_{eq}}$), and normalized perimeter ($\overline{P_{nor}}$) are summarized in Table 1 for recrystallized quartz grains in each subdomain from the analyzed quartz schist samples. The average equivalent diameters ($\overline{D_{eq}}$) vary between 38-92 μm in different domains from the analyzed samples (Table 1). It should be noted that the average equivalent diameters are coarser in less sheared samples (Nishi-1, Nishi-4) varying between 74-92 μm than in more sheared samples (Nishi-2, Nishi-3) varying between 38-61 μm. While the average equivalent diameters are comparable between the less (R) and more sheared (S) domains of sample Nishi-2 (53-57 μm), those in the former domain (55-61 μm) is slightly coarser than those in the latter domain (38-42 μm) of sample Nishi-3. The average equivalent diameters in sample Nishi-5 (52-61 μm) are comparable with those in sample Nishi-2 and the less sheared domain of sample Nishi-3. The average aspect ratios ($\bar{R}$) for all the domains from different samples

little vary between 1.7-2.2, which can be correlated with *P*-type recryatallized grains after Masuda and Fujimura (1981). Also considering that lobate grain boundaries indicative of grain-boundary migration recrystallization are dominant (Fig. 6a), the analyzed recryatalized quartz grains were perhaps originally formed in grain-boundary migration regime after Stipp et al. (2002).

Here, it is noted that recrystallized quartz grains for which *c*-axis orientations were measured and those for which microstructural analyses were conducted are not completely correlated. Hence, *FI* is treated as the same between subdomains from a domain or domains (only for the case of domains Nishi-5-A, B), where the quartz *c*-axis fabric was measured (also see Table 1).

The average normalized perimeter ($\overline{P_{nor}} = \bar{P}/\overline{P_{eq}}$) in different domains from all the samples, which vary between 1.09 to 1.17, are well correlated with the intensity of quartz *c*-axis fabrics (*FI*), although the average normalized perimeters for different subdomains are greatly scattered for domains Nishi-5-A, B with a random quartz *c*-axis fabric (Fig. 9). According to the calculated high *T*-value (3.764, Table 2), it can be concluded that the hypothesis that the two indices, $\overline{P_{nor}}$ and *FI* are not correlated at all is rejected with the risk ratio less than 0.0025 (see Appendix A for explanation).

These results of image analyses are completely consistent with microstructural occurrences that recrystallized quartz grains in domains with a well-defined type I crossed girdle quartz *c*-axis pattern

show ellipsoidal shape with lobate grain boundaries (e.g. Fig. 6a), while those with a random *c*-axis fabric show irregular shape with more straight grain boundaries (Figs. 6f, g). Straight grain boundaries are formed by pinning of grain boundaries on mica, which becomes more dominant as the intensity of quartz *c*-axis fabrics decreases from strong through weak to random ones.

The R/ϕ diagrams (e.g. Ghosh, 1993) are constructed for all the domains from different samples, and divided into three groups with the different quartz *c*-axis fabric intensities (i.e. strong, weak, and random ones, Fig. 10). It is clear from these diagrams that a well-defined SPO of recrystallized quartz grains develops in domains with a strong quartz *c*-axis fabric. However, SPO becomes weak as the fabric intensity decreases from strong through weak to random quartz *c*-axis fabrics, although this is not clearly discerned in some samples (e.g. in Nishi-2, those for domains R and S are not much different). Also, in most of domains with a strong or weak quartz *c*-axis fabric, the majority of long-axis orientations is commonly shifted toward the negative side with the orientation of highest *R* located at ϕ= -10 to -20^{o} (Figs. 10a, b), defining an oblique foliation of recrystallized quartz grains (e.g. Passchire and Trouw, 1996). The oblique foliation suggests a top-to-the-west sense of shear, which conforms to that inferred from the asymmetric quartz *c*-axis fabric patterns in these domains. On the other hand, it should be noted that only SPOs in sample Nishi-5 exhibit a very-weak pattern, where most of ϕ's are in the positive side (Fig. 10c). This pattern is not comparable with those with a

single peak at a small negative ϕ value from the other samples, which are formed by crystal plastic deformation in quartz aggregates.

5.4. Area fraction of mica

The results of area fraction of mica are shown in Table 1, and also the diagrams of average normalized perimeter ($\overline{P_{nor}}$) versus mica fraction (*MF*) and fabric intensity (*FI*) versus mica fraction (*MF*) have been constructed (Fig. 11). As one can see from Table 1 and Fig. 11, the area fraction of mica varies between 1.7 to 8.2 %, which increases with decreasing normalized perimeter (Fig. 11a) and decreasing fabric intensity (Fig. 11b). Again, whether or not both $\overline{P_{nor}}$ and *MF*, and *FI* and *MF* are in fact correlated are evaluated with the risk ratio (see Appendix A). Based on the calculated *T*-values for both correlations (2.583 and 4.048, Table 2), the hypotheses that the two indices are not correlated at all are rejected with the risk ratios less than 0.01 for the former, and 0.0025 for the latter cases of correlation, respectively.

6. Discussion

6.1. Microstructural development in the quartz schist samples caused by coupled micro-faulting and pressure solution creep during the D_2 stage

It is extraordinary that in the quartz schist samples from the Niihama area, the density of shear bands correlated with outcrop-scale D_2 low-angle normal faults is very high, and the quartz *c*-axis fabrics are weak or random in some of the samples. First of all, D_2 low-angle normal faulting and associated formation of shear bands occurred under the conditions of frictional-viscous transition of quartz (c. 300 ^{o}C, e.g. Takeshita, 1995; Stöckhert et al., 1999), based on the occurrence of both brittle (i.e. shear bands) and ductile (i.e. deformation bands, Fig. 6b) microstructures in deformed quartz schist. Such microstructural features are rarely observed in quartz schist samples from the other localities in central Shikoku such as the Asemi river area, where strong quartz *c*-axis fabrics were pervasively developed by dislocation creep at the D_1 stage (e.g. Wallis, 1990, 1995; Sakakibara et al., 1992; Wallis et al., 1992; Yagi and Takeshita, 2002; Takeshita and Yagi, 2004). On the other hands, Vidal et al. (2006) showed that the development of shear bands at temperature conditions of 200-300 ^{o}C was extensive in some pelitic schist from the the Asemi river area, which can be correlated with D_2 shear bands in both quartz schist and pelitic schist from the Niihama area. Hence, although D_2 deformation was in fact very strong in the Niihama area, it was penetrative in the whole

Sambagawa schist in central Shikoku (also see Takeshita and Yagi, 2004; El-Fakharani and Takeshita, 2008).

It should be noted that the D_1 strong quartz *c*-axis fabrics are preserved in lenses consisting of coarse-grained quartz aggregates bounded by shear bands (domains Nishi-1-A, Nishi-2-R, Nishi-3-R, Nishi-4-A, Fig. 8), even though the density of shear bands is high in these samples. However, in the fairly sheared quartz lenses (Nishi-2-S and Nishi-3-S), although the skeleton of type I crossed girdle quartz *c*-axis fabric is still preserved, their intensities are lower than those in the less sheared quartz lenses (Nishi-2-R and Nishi-3-R). Further, in domains A and B from sample Nishi-5, quartz *c*-axis fabric is completely random. Therefore, although these rocks were pervasively sheared at D_2 stage during the exhumation across the depth of frictional-viscous transition of quartz, leading to the dominant development of shear bands in the analyzed quartz schist samples, D_1 quartz *c*-axis fabrics are essentially preserved in lenses surrounded by D_2 shear bands. On the other hand, the reason why quartz *c*-axis fabric became weak and finally random with increasing amount of shear will be discussed below.

It is noted that the normalized perimeter ($\overline{P_{nor}}$) decreases as the area fraction of mica (*MF*) increases (Fig. 11a) in quartz lenses surrounded by shear bands in the analyzed samples. This can be explained by the fact that more recrystallized quartz grains become bounded by mica flake, thus

increasing the portion of straight grain boundaries with increasing area fraction of mica, which is consistent with microstructural observation under a microscope. Further, the intensity of quartz *c*-axis fabric (*FI*) decreases as the average normalized perimeter of recrystallized quartz grains ($\overline{P_{nor}}$) decreases and the area fraction of mica (*MF*) increases (Figs. 9, 11b). It should be further noted that intracrystalline microstructures change as both ($\overline{P_{nor}}$) and *MF* change. Other than lobate grain boundaries indicative of grain-boundary migration recrystallization being replaced by straight grain boundaries, wavy extinction and kink bands formed by dislocation creep at D_1 stage become less developed with decreasing $\overline{P_{nor}}$ and increasing *MF*. This has been also evidenced by analyses of dislocation substructures, where sub-boundaries (i.e. optically kink bands) are abundant in recrystallized quartz grains with higher $\overline{P_{nor}}$ and lower *MF* from a less sheared quartz lens, while these substructures are absent in those with lower $\overline{P_{nor}}$ and high *MF* from a strongly sheared quartz lens. Further, SPOs in sample Nishi-5 with a random *c*-axis fabric show a very-weak pattern (Fig. 10c), which is unlikely to have been formed by crystal plastic deformation of quartz aggregates. Based on these facts mentioned above, it is inferred that the obliteration of strong quartz *c*-axis fabrics formed at the D_1 stage was most probably caused by dissolution of existing quartz grains and precipitation of randomly oriented new quartz grains from the solution during pressure solution creep. Here, although it has been reported that a weak *X*-maximum quartz *c*-axis fabric was

developed during dissolution-precipitation creep of quartz (e.g. Hippertt, 1994; Takeshita and Hara, 1998), randomization of the existing quartz *c*-axis fabric caused by intracrystalline plasticity could be a more general microstructural development at a low degree of phyllonitization of quartzite (see fig. 12 of Hippertt, 1994).

Dissolution of quartz is extensive at quartz-mica interface, in particular, at quartz lens-micro-shear zone interface (i.e. truncation of recrystallized quartz grains, Fig. 6e), leading to the straight interphase boundaries. Although there is no direct evidence for precipitation of the new quartz grains, the straight interphase boundaries normal to the foliation (Fig. 6g) indicate that growing quartz grains by precipitation were pinned by mica. Also, since dilation in the samples was caused during D_2 semi-brittle deformation, shown by precipitation of chlorite, quartz could also have been precipitated from the solution in dilatant spaces. Furthermore, in some quartz grains from a sheared domain of sample Nishi-2 (Nishi-2-S), dislocations are not tangled, their densities are low and subboundaries are absent, indicating that these grains are perhaps newly precipitated grains from the solution, which experienced only a small amount of intracrystalline deformation. Hence, pervasive micro-faulting (i.e. formation of shear bands) in the analyzed quartz schist samples did not operate alone, and rather was accommodated by pressure solution in quartz, which has been theoretically demonstrated for fault rocks consisting of quartz-mica aggregates based on analog

experiments on halite-kaolinite mixture (Bos and Spiers, 2002).

Microstructures of sample Nishi-5 are distinct from those of the other samples on the points of completely random quartz *c*-axis fabric, irregular quartz grain boundaries with more straight boundaries pinned by mica, little wavy extinction and kink bands in quartz grains, and higher area fraction of mica. Further, this sample does not exhibit a quartz lens-sheared matrix microstructure, although micro-shear zones are less frequently observed (Fig. 6f). The quartz microstructures of sample Nishi-5 (Figs. 6f, g) is also reminiscent of those in a recrystallized quartz vein with a weak *X*-maximum *c*-axis fabric component reported by Takeshita and Hara (1998) (their fig. 6a), where pressure solution creep pervasively occurred. On the other hand, in the same quartz vein, dislocation creep shown by formation of subgrains and recrystallized grains by subgrain rotation also operated in some domains. Takeshita and Hara (1998) interpreted that there is a local difference in differential stress even at a thin section scale, and dislocation creep and pressure solution creep dominate in domains under relatively high and low differential stress, respectively. Accordingly, it is inferred that sample Nishi-5 was placed under lower differential stress, where pressure solution pervasively occurred with less development of shear bands and micro-shear zones, while the other samples were placed under higher differential stress, where micro-faulting extensively occurred with more development of these microstructures.

6.2. Possible large degree of weakening by coupled micro-faulting and pressure solution creep

A critical drawback of the frictional-viscous model for the upper crustal rheology is that the estimate of strength for frictional sliding is based on the strength of pre-existing fault surfaces in non-fault rocks (i.e. Byerlee's law). On the other hand, structural geologists have known that most of the strain in the brittle upper part of the upper crust was accommodated by the displacement along major faults with a wide shear zone. Then, it has been proposed that low strain-rate stable sliding accommodated by pressure solution occurred in phyllosilicate-bearing fault rocks under stresses far below those based on the Byerlee's law (e.g. Bos and Spiers, 2002). Also, similar type of faulting could have occurred along fault plane decorated by quartz slickenfiber (Gratier and Gueydan, 2007).

In the following, the large degree of weakening which could have occurred in the analyzed quartz schist deformed at frictional-viscous transition regions will be discussed, referring to the recent model of coupled micro-faulting and pressure solution creep (or frictional-viscous flow, Bos and Spiers, 2002, Fig. 12). In the model of frictional-viscous flow, the strength of rocks is contributed by both frictional sliding along phyllosilicate layers or within those (slider, element A) and pressure solution of quartz (dashpot, element B), because elements A and B are connected in

parallel (Voigt model). This rheology model is in fact applicable to the present sheared quartz schist samples, where coupled micro-faulting and pressure solution creep in fact occurred. Although in this scheme, the total strength of rocks is the sum of those of elements A and B, and is controlled by the strength of stronger element, in the real situation, the strength could be approximated by the intermediate model between the Voigt and Maxwell models, and hence the total strength of rocks could be in between those of elements A and B.

Then, we have to consider the strength of each element. The strength for frictional sliding (element A) can be modeled as the normal stress multiplied by the coefficient of internal friction, which little depends on strain rate. Whereas the value of 0.6-0.85 is used for the coefficient of internal friction in the classical model of crustal strength (Byerlee's law), in the new model, the value of 0.2 is used based on e.g. experimentally determined frictional coefficient for kaolinite gouge (Bos and Spiers, 2002). This makes 3 to 4 times strength decrease for frictional sliding with respect to that for the classical one, which is in fact likely for rheology in the present micro-shear zone consisting of very-fine-grained quartz aggregates and aligned mica.

Pressure solution of minerals is a composite process consisting of dissolution, diffusion and precipitation under the presence of fluid, and rate-controlling processes have been debated; i.e. they are either grain boundary diffusion-controlled, or dissolution or precipitation-controlled (e.g. Spiers

and Schutjens, 1990; Shimizu, 1995; van Noort et al., 2008). The rate of pressure solution is proportional to differential stress (σ), and as for the grain size sensitivity of strain rate, $\dot{\varepsilon} \propto \frac{\sigma}{d^3}$ for grain boundary diffusion-controlled pressure solution, and $\dot{\varepsilon} \propto \frac{\sigma}{d}$ for dissolution or precipitation-controlled pressure solution. Here, $\dot{\varepsilon}$ and *d* are strain rate and diameter of a grain, respectively. Both Gratier (1993) and Gratier and Gueydan (2007) conducted pressure solution creep experiments on halite with saturated brine, and showed that pressure solution creep is rate-controlled by diffusion, based on the large increase in strain rate due to the reduction of diffusion-path length by microfracturing.

On the other hand, it has been recently shown by experiments that pressure solution of quartz is greatly enhanced at the quartz-mica interphase boundary under a very small amount of differential stress of 0.2-0.3 MPa, driven by the electrical potential difference, whereas that at quartz-quartz boundary is negligible (Greene et al., 2009). These new experimental findings on the driving force of pressure solution in fact accord with the natural observations not only in the present study, but also in literature (e.g. Hippertt, 1994; Takeshita and Hara, 1998), where pressure solution of quartz seems to be greatly enhanced at the quartz-mica interphase boundary.

In the present quartz schist samples, shear bands (i.e. microfractures) decorated by newly grown aligned mica were principal fluid path-ways. Hence, the formation of shear bands alone contributes

to the reduction of creep strength by pressure solution, by reducing the diffusion path length (Gratier et al., 1999; Gratier and Gueydan, 2007). Further, the formation of micro-shear zones consisting of very-fine-grained quartz aggregates and aligned mica led to the great reduction of creep strength by pressure solution, because the strain rate is strongly dependent on the grain size. Furthermore, if pressure solution occurs driven by the elecrtrochemical effect at the interphase boundary under a very low differential stress, the increasing amount of mica, which was newly grown along shear bands or in micro-shear zones, could have greatly reduced the creep strength by pressure solution (Greene et al., 2009). The inference is consistent with the fact that the degree of pressure solution shown by the degree of obliteration of existing quartz *c*-axis fabrics increases with the increasing amount of mica in the present sheared quartz schist samples (Fig. 11b).

Microstructural development and increasing importance of pressure solution creep with increasing shear strain in the present quartz schist sample is schematically drawn in Fig. 13. Initially at stage 1, for the formation of shear bands and micro-shear zones, very-high differential stresses were perhaps required shown by the very-fine sizes of dynamically recrystallized quartz grains formed along them (Fig. 6c, see e.g. Twiss, 1986 for the relation between differential stress and recrystallized grain size). Subsequently, deformation in the micro-shear zones was perhaps accommodated by coupled micro-faulting and pressure solution creep under low differential stresses,

because of both low coefficient of internal friction of mica and very-small grain sizes of recrystallized quartz grains. As a result, differential stresses became more concentrated in quartz lenses with increasing volume fraction of micro-shear zones, which resulted in further micro-faulting in the quartz lenses (Rs in stage 2 of Fig. 13). This microstructural development is analogous to that of multi-scale shear zones at the frictional-viscous transition zones analyzed by Fusseis et al. (2006) and Schrank et al. (2008). With further increasing volume fraction of micro-shear zones, each of the quartz lenses became isolated, when they no longer behaved as a load-bearing framework, which led to a great reduction of differential stresses in them **(**Ss in stage 2 of Fig. 13**)**. The differential stresses, σ inferred from dislocation density, ρ (i.e. $\sigma \propto \sqrt{\rho}$, e.g. Twiss, 1986) are significantly lower in recrystallized quartz grains from the sheared lens than those from the relatively unsheared one (i.e. relict grains). The lower differential stresses recorded in the former grains under frictional-viscous transition conditions at D_2 phase, which are expected to be higher than those recorded in the latter grains deformed in fully ductile regime at D_1 phase, strongly suggest that the strength was greatly reduced from the peak differential stresses for the formation of shear bands during D_2 phase. This is perhaps attributed to the fact that pressure solution creep, which becomes dominant at lower differential stresses than frictional sliding and dislocation creep (e.g. Passchier and Trouw, 1996), was greatly enhanced due to the increases in density of shear bands and mica fraction (cf. Stewart et

al., 2000).

This microstructural development could have finally led to the situation, where most of the strain was accommodated by pressure solution in both quartz lenses and micro-sheared zones (i.e. matrices) under very low differential stresses (stage 3 of Fig. 13). If stage 3 directly follows stage 1 or is reached after the formation of large volume fraction of micro-sheared zones (stage 2) depends on the magnitude of differential stresses (Fig. 13). At this stage, the amount of shear strain by pressure solution became enormous, which led to the complete randomization of quartz *c*-axis fabrics in the quartz lenses as those in sample Nishi-5.

7. Conclusions

Microstructural analyses have been conducted for quartz schist samples from the Sambagawa metamorphic rocks, Niihama-area, southwest Japan. In these samples, very strong quartz *c*-axis fabrics characterized by asymmetrical type-I crossed girdles and associated microstructures were once developed at D_1 phase by crystal plastic deformation during exhumation, which were overprinted by pervasive D_2 normal faulting at the conditions of frictional-viscous transition of quartz (*c.* 300 ^{o}C) during further exhumation into the upper crustal level. Due to this brittle normal

faulting, quartz schist samples were pervasively sheared, resulting in the formation of numerous shear bands, along which phengite mica was newly precipitated from the solution. Some of shear bands were further developed into micro-shear zones, which consist of very-fine-grained quartz aggregates and newly grown aligned mica parallel to these, leading to quartz lens-micro-shear zone (i.e. matrix) microstructures in highly sheared quartz schist.

Although both relict quartz *c*-axis fabrics and microstructures indicating crystal plastic deformation are essentially preserved in less sheared domains of the quartz lenses, they become weak and finally random in highly sheared domains. Various microstrucural indices of recrystallized quartz grains such as grain size, perimeter and aspect ratio were quantitatively analyzed with an image analysis software (NIH-Image). It has been found that the intensity of quartz *c*-axis fabrics decreases with the decreasing degree of undulation of recrystallized grain boundaries, which is calculated as the average perimeter divided by that of fitted ellipse (i.e. average normalized perimeter). The average normalized perimeter in turn decreases with increasing area fraction of newly precipitated mica from the solution. These facts are interpreted as caused by increasing activity of pressure solution: the relict recrystallized quartz grains seem to have been dissolved mostly at quartz-platy mica interface, new quartz grains with random crystallographic orientations were precipitated and pinned by mica, thus increasing the portion of straight boundaries of

recrystallized quartz grains (i.e. reduction of the average normalized perimeter).

In the sheared quartz schist samples, the shear deformation was perhaps accommodated by coupled micro-faulting and pressure solution, as suggested by Bos and Spiers (2002), and the total strength of rocks became reduced by increasing number of shear bands, which caused the reduction of diffusion path length, leading to the increasing rate of pressure solution. With further increasing shear deformation, the strain became more accommodated by pressure solution in micro-shear zones, and the quartz lenses were further sheared by the resultant stress concentration, leading to the increasing volume fraction of micro-shear zones (cf. Fusseis et al, 2006; Schrank et al., 2008). At this microstructural setting with plenty of mica, pressure solution pervasively occurred at the quartz-mica interface even under very low differential stresses driven by the electrical potential difference (Greene et al., 2009), which led to a complete obliteration of existing quartz *c*-axis fabrics in some quartz schist.

Acknowledgements

We thank S. Motai, A. Okamoto and T. Nakayama for assistance in analyses with a TEM. We acknowledge K. Kanagawa and an anonymous reviewer for constructive reviews, which greatly

improved the manuscript.

Appendix A. Correlation of two indices evaluated by the risk ratio

In this paper, whether or not two indices are correlated, is evaluated by the risk ratio. Assuming that each of two indices exhibits a normal distribution, and that these are not correlated at all, the following value *T*, which is calculated from the correlation constant (*C*) as shown below, follows the Student *t*-distribution of *n*-2 degree of freedom (mentioned in most of textbooks of statistics).

$$T = \sqrt{\frac{(n-2)C^2}{1-C^2}} \quad \text{(A1)}$$

where *n* is the number of samples. Then, the risk ratio is defined by the area (α), which is the integrated value of the *t*-distribution from *T* to infinity. The square of calculated correlation constant (C^2) and *T*-value between two indices analyzed in this study are shown in Table 2.

References

Allemendinger, R. W., 1988. Stereonet 4.9.5. Academic version; a plotting program for orientation data. Computer Program.

Banno, S., Sakai, C., 1989. Geology and metamorphic evolution of the Sanbagawa metamorphic belt, Japan. In: Daly, J. S., Cliff, R. A., Yardley, B. W. D. (Eds.), Evolution of Metamorphic Belts. Geological Society, London, Special Publications, 43, pp. 519-532.

Banno, S., Sakai, C., Higashino, T., 1986. Pressure-temperature trajectory of the Sanbagawa metamorphism deduced from garnet zoning. Lithos 19, 51-63.

Banno, S., Higashino, T., Otsuki, M., Itaya, T., Nakajima, T., 1978. Thermal structure of the Sanbagawa metamorphic belt in central Shikoku. Journal of Physics of the Earth 26 (Suppl.), 345-356.

Banno, Y., 2000. Intermediate high-pressure exhumation of the northern segment of the Sanbagawa belt, Saruta-gawa area, central Shikoku, Japan. Lithos 50, 289-303.

Beaumont, C., Jamieson, R. A., Nguyen, M. H., Medvedev, S., 2004. Crustal channel flow: 1. Numerical models with applications to the tectonics of the Himalayan-Tibetan orogen. Journal of Geophysical Research 109, B06406. doi:10.1029/2003JB00280.

Bos, B., Spiers, C. J., 2002. Frictional-viscous flow of phyllosilicate-bearing fault rocks: Microphysical model and implications for crustal strength profiles. Journal of Geophysical Research 107, 1-13, doi: 10.1029/2001JB000301.

Brown, M., **1998**. Unpairing metamorphic belts: *P-T* paths and a tectonic model for the Ryoke Belt, southwest Japan. Journal of Metamorphic Geology 16, 3-22.

Byerlee, J., 1978. Friction of rocks. Pure and Applied Geophysics 116, 615-627.

Duebendorfer, E. M., Vermilye, J., Geiser, P. A., Davis, T. L., 1988. Evidence for aseismic deformation in the western Transverse Ranges, Southern California: Implications for seismic risk assessment. Geology 26, 271-274.

El-Fakharani, A.-H., Takeshita, T., 2008. Brittle normal faulting in the highest-grade Sambagawa metamorphic rocks of central Shikoku, southwest Japan: Indication of the exhumation into the upper crustal level. Journal of Asian Earth Sciences 33, 303-322.

Enami, M., Wallis, S. R., Banno, Y., 1994. Paragenesis of sodic pyroxene-bearing quartz schists: implications for *P-T* history of the Sanbagawa belt. Contributions to Mineralogy and Petrology 116, 182-198.

Faure, M., 1983. Eastward ductile shear during the early tectonic phase in the Sanbagawa belt. Journal of Geological Society of Japan 89, 319-329.

Faure, M., 1985. Microtectonic evidence for eastward ductile shear in the Jurassic orogen of SW Japan. Journal of Structural Geology 7, 175-186.

Faure, M., Iwasaki, M., Ichikawa, K., Yao, A., 1991. The significance of Upper Jurassic radiolarians in high pressure metamorphic rocks of SW Japan. Journal of Southwest Asian Earth Sciences 6, 131-136.

Fukunari, T., Wallis, S. R., 2007. Structural evidence for large-scale top-to-the-north normal displacement along the Median Tectonic Line in southwest Japan. Island Arc 16, 243-261.

Fusseis, F., Handy, M. R., Schrank, C. E., 2006. Networking of shear zones at the brittle-to-viscous transition (Cap de Creus, NE Spain). Journal of Structural Geology 28, 1228-1243.

Ghosh, S. K., 1993. Structural geology: Fundamentals and modern developments. Pergamon Press, Oxford, 598pp.

Gratier, J. P., 1993. Experimental pressure solution of halite by an indenter technique. Geophysical

Research Letters 20, 1647-1650.

Gratier, J. P., Renard, F., Labaume, P., 1999. How pressure solution creep and fracturing processes interact in the upper crust to make it behave in both a brittle and viscous manner. Journal of Structural Geology 21, 1189-1197.

Gratier, J. P., Gueydan, F., 2007. Deformation in the presence of fluids and mineral reactions: Effect of fracturing and fluid-rock interaction on seismic cycles. In: Handy, M., Hirth, G., Hovius, N. (Eds.), Tectonic Faults: Agents of change on dynamic Earth. The MIT Press, Cambridge, Massachusetts, pp. 319-356.

Greene, G., Kristiansen, K., Meyer, E. E., Boles, J., Israelachvili, J. N., 2009. Role of electrochemical reactions in pressure solution. Geochimica et Cosmochimica Acta 73, 2862-2874.

Hara, I., Hide, K., Takeda, K., Tsukuda, E., Tokuda, M., Shiota, T., 1977. Tectonic movement in the Sambagawa belt. In: Hide, K. (Ed.), The Sambagawa Belt, Hiroshima University Press, Hiroshima, pp. 307-390 (in Japanese with English abstract).

Hara, I., Shiota, T., Hide, K., Okamoto, K., Takeda, K., Hayasaka, Y., Sakurai, Y., 1990. Nappe structure of the Sambagawa belt. Journal of Metamorphic Geology 8, 441-456.

Hara, I., Shiota, T., Hide, K., Kanai, K., Goto, M., Seki, S., Kaikiri, K., Takeda, K., Hayasaka, Y., Miyamoto, T., Sakurai, Y., Ohtomo, Y., 1992. Tectonic evolution of the Sambagawa schists and its implications in convergent margin processes. Journal of Science of the Hiroshima University, Series C 9, 495-595.

Higashino, T., 1990. The higher grade metamorphic zonation of the Sambagawa metamorphic belt in central Shikoku, Japan. Journal of Metamorphic Geology 8, 413-423.

Hippertt, J. F., 1994. Microstructures and *c*-axis fabrics indicative of quartz dissolution in sheared

quartzites and phyllonites. Tectonophysics 229, 141-163.

Isozaki, Y., Itaya, T., 1990. Chronology of Sanbagawa metamorphism. Journal of Metamorphic Geology 8, 401-411.

Itaya, T., Takasugi, H., 1988. Muscovite K-Ar ages of the Sanbagawa schists, Japan and argon depletion during cooling and deformation. Contributions to Mineralogy and Petrology 100, 281-290.

Kohlstedt, D. L., Evans, B., Mackwell, S. J., 1995. Strength of the lithosphere: Constraints imposed by laboratory experiments. Journal of Geophysical Research 100, 17,587-17,602.

Lachenbruch, A. H., Sass, J. H., 1992. Heat flow from Cajon Pass, fault strength, and tectonic implications. Journal of Geophysical Research 97, 4995-5015.

Law, R. D., 1987. Heterogeneous deformation and quartz crystallographic fabric transitions: natural examples from the Moine Thrust zone at the stack of Glencoul, northern Assynt. Journal of Structural Geology 9, 819-833.

Lisle, R. J., 1985. The use of the orientation tensor for the description and statistical testing of fabrics. Journal of Structural Geology 7, 115-117.

Lister, G. S., 1977. Discussion: Crossed girdle *c*-axis fabrics in quartzites plastically deformed by plane strain and progressive simple shear. Tectonophysics 39, 51-54.

Masuda, T., Fujimura, A., 1981. Microstructural development of fine-grained quartz aggregates by syntectonic recrystallization. Tectonophysics 72, 105-128.

Miyashiro, A., 1961. Evolution of metamorphic belts. Journal of Petrology 2, 277-331.

Nakamura, C., Enami, M., 1994. Prograde amphiboles in hematite-bearing basic and quartz schists in the Sanbagawa belt, central Shikoku: relationship between metamorphic field gradient and *P-T* paths of individual rocks. Journal of Metamorphic Geology 12, 841-852.

Nakashima, S., 1995. Diffusivity of ions in pore water as a quantitative basis for rock deformation rate estimates. Tectonophysics 245, 185-203.

National Institute of Health, 1999. NIH Image 1.62, public domain image analysis software. National Technical Information Service, Springfield, Virginia.

Niemeijer, A. R., Spiers, C. J., **2005**. Influence of phyllosilicates on fault strength in the brittle-ductile transition: insight from rock analogue experiments. In: Bruhn, D., Burlini, L., (Eds.), High-Strain Zones: Structures and Physical Properties. Geological Society, London, Special Publications, 245, pp. 303-327.

Okamoto, A., Toriumi, M., 2004. Optimal mixing properties of calcic and subcalcic amphiboles: application of Gibbs' method to th Sanbagawa schists, SW Japan. Contributions to Mineralogy and Petrology 146, 529-545.

Okamoto, K., Shinjoe, H., Katayama, I., Terada, K., Sano, Y., Johnson, S., 2004. SHRIMP U-Pb dating of quartz-bearing eclogite from the Sanbagawa Belt, south-west Japan: implication for metamorphic evolution of subducted protolith. Terra Nova 16, 81-89.

Osozawa, S., Pavlis, T., 2007. The high *P/T* Sambagawa extrusional wedge, Japan. Journal of Structural Geology 29, 1131-1147.

Passchier, C. W., Trouw, R. A. J., 1996. Microtectonics. Springer-Verlag, Berlin, 289pp.

Ramsay, J. G., 1967. Folding and Fracturing of Rocks. McGraw-Hill, New York, 568pp.

Sakakibara, N., Hara, I., Kanai, K., Kaikiri, K., Shiota, T., Hide, K., Paulitsch, P., 1992. Quartz microtextures of the Sambagawa schists and their implications in convergent margin processes. Island Arc 1, 175-192.

Sakashima, T., Terada, K., Takeshita, T., Sano, Y., 2003. Large-scale displacement along the Median Tectonic Line, Japan: evidence from SHRIMP zircon U-Pb dating of granites and gneisses from

the South Kitakami and paleo-Ryoke belts. Journal of Asian Earth Sciences 21, 1019-1039.

Schrank, C. E., Handy, M. R., Fusseis, F., 2008. Multiscaling of shear zones and the evolution of the brittle-to-viscous transition in continental crust. Journal of Geophysical Research 113, B01407, doi:10.1029/2006JB004833.

Shimizu, I., 1995. Kinetics of pressure solution creep in quartz: theoretical considerations. Tectonophysics 245, 121-134.

Shiota, T., Hara, I., Seki, S., Ikeda, Y., Okudaira, T., Hide, K., 1993. Sinistral enéchelon folding of the Sambagawa schists and its tectonic implication. Journal of Science of the Hiroshima University, Series C 9, 671-683.

Spiers, C. J., Schutjens, P. M. T. M., 1990. Densification of crystalline aggregates by fluid phase diffusion creep. In: Barber, D. J., Meredith, P. G. (Eds.), Deformation Processes in Minerals, ceramics and Rocks. Unwin Hyman, London, pp. 334-353.

Stewart, M., Holdsworth, R. E., Strachan, R. A., 2000. Deformation processes and weakening mechanisms within the frictional-viscous transition zone of major crustal-scale faults: insights from the Great Glen Fault Zone, Scotland. Journal of Structural Geology 22, 543-560.

Stipp, M., Stunitz, H., Heilbronner, R., Schmid, S. M., 2002. The eastern Tonale fault zone: a 'natural laboratory' for crystal plastic deformation of quartz over a temperature range from 250 to 700 ^{o}C. Journal of Structural Geology 24, 1861-1884.

Stöckhert, B., 2002. Stress and deformation in subduction zones: insight from the record of exhumed metamorphic rocks. In: de Meer, S., Drury, M. R., de Bresser, J. H. P., Pennock, G. M. (Eds.), Deformation Mechanisms, Rheology and Tectonics: Current Status and Future Perspectives. Geological Society, London, Special Publications, 200, pp. 255-274.

Stöckhert, B., Brix, M. R., Kleinschrodt, R., Hurford, A. J., Wirth, R., 1999. Thermochronometry

and microstructures of quartz – a comparison with experimental flow laws and predictions on the temperature of the brittle-plastic transition. Journal of Structural Geology 21, 351-359.

Tagami, M., Takeshita, T., **1998**. *c*-Axis fabrics and microstructures in quartz schist from the Sambagawa metamorphic belt, central Shikoku, Japan. Journal of Structural Geology 20, 1549-1568.

Taira, A., Tokuyama, H., Soh, W., 1989. Accretion tectonics and evolution of Japan. In: Ben-Avraham, Z. (Ed.), The Evolution of the Pacific Ocean Margins. Oxford University Press, Oxford, pp. 100-123.

Takasu, A., Dallmeyer, R. D., 1990. $^{40}Ar/^{39}Ar$ mineral age constraints for the tectonothermalevolution of the Sambagawa metamorphic belt, central Shikoku, Japan: a Cretaceous accretionary prism. Tectonophysics 185, 111-139.

Takasu, A., Wallis, S., Banno, S., Dallmeyer, R. D., 1994. Evolution of the Sambagawa metamorphic belt, Japan. Lithos 28, 69-84.

Takeshita, T., 1995. Dynamic analysis of deformed quartz grains from the folded Middle Miocence Momonoki Subgroup of central Japan: origin of healed microcracks. Tectonophysics 245, 277-297.

Takeshita, T., Hara, I., 1998. *c*-Axis fabrics and microstructures in a recrystallized quartz vein deformed under fluid-rich greenschist conditions. Journal of Structural Geology 20, 417-431.

Takeshita, T., Yagi, K., 2004. Flow patterns during exhumation of the Sambagawa metamorphic rocks, southwest Japan, caused by brittle-ductile, arc-parallel extension. In: Grocott, J., McCaffrey, K. J. W., Taylor, G., Tikoff, B. (Eds.), Vertical Coupling and Decoupling in the Lithosphere. Geological Society, Special Publications, London, 227, pp. 279-296.

Toriumi, M., Teruya, J., Masui, M., H. Kuwahara, 1986. Microstructures and flow mechanisms in

regional metamorphic rocks of Japan. Contributions to Mineralogy and Petrology 94, 54-62.

Twiss, R. J., 1986. Variable sensitivity piezometric equations for dislocation density and subgrain diameter and their relevance to olivine and quartz. In: Hobbs, B. E., Heard, H. C. (Eds.), Mineral and Rock Deformation: Laboratory Studies. The Paterson Volume. Geophysical Monograph 36, American Geophysical Union, Washington, D. C., pp. 247-261.

Van Noort, R., Spiers, C. J., Pennock, G. M., 2008. Compaction of granular quartz under hydrothermal conditions: Controlling mechanisms and grain boundary processes. Journal of Geophysical Research 113, B12206, doi: 10.1029/2008JB005815.

Vidal, O., de Andrade, V., Lewin, E., Munoz, M., Parra, T., Pascarelli, S., 2006. P－T-deformation-Fe^{3+}/Fe^{2+} mapping at thin section scale and comparison with XANES mapping: application to garnet-bearing metapelite from the Sambagawa metamorphic belt (Japan). Journal of Metamorphic Geology 24, 669-683.

Wallis, S. R., 1990. The timing of folding and stretching in the Sambagawa belt: the Asemigawa region, central Shikoku. Journal of Geological Society of Japan 96, 345-352.

Wallis, S. R., 1995. Vorticity analysis and recognition of ductile extension in the Sanbagawa belt, SW Japan. Journal of Structural Geology 17, 1077-1093.

Wallis, S. R., Banno, S., Radvanec, M., 1992. Kinematics, structure and relationship to metamorphism of the east-west flow in the Sanbagawa Belt, southwest Japan. Island Arc 1, 176-185.

Wintsch, R. P., Byrne, T., Toriumi, M., 1999. Exhumation of the Sanbagawa blueschist belt, SW Japan, by lateral flow and extrusion: evidence from structural kinematics and retrograde *P-T-t* paths. In: Ring, U., Brandon, M. T., Lister, G. S., Willet, S. D. (Eds.), Exhumation processes: Normal Faulting, Ductile Flow and Erosion. Geological Society, London, Special Publications,

154, pp. 129-155.

Woodcock, N. H., **1977**. Specification of fabric shapes using an eigenvalue method. Geological Society of America Bulletin 88, 1231-1236.

Yagi, K., Takeshita, T., 2002. Regional variation in exhumation and strain rate of the high-pressure Sambagawa metamorphic rocks in central Shikoku, southwest Japan. Journal of Metamorphic Geology 20, 633-647.

Figure captions

Fig. 1. (a) Simplified index map of SW Japan and Shikoku Island. (b) Metamorphic zonation map of the Sambagawa metamorphic belt, central Shikoku. Modified after Higashino (1990). Arrows indicate the average movement direction of the upper plate by D_2 normal faulting inferred from quartz slickenfibre or striation on minor normal faults investigated in each area (shown by a frame, El-Fakharani and Takeshita, 2008). (c) Cross-section across central Shikoku (Kamio-Asemi river section). Modified after Banno et al. (1978, 1986), Takasu and Dallmeyer (1990) and Takasu et al. (1994), incorporating the inferred D_2 major normal fault (denoted by "F" in (b)) proposed by El-Fakharani and Takeshita (2008). In (b), the traverse line (I-I') of the cross-section is shown. MTL, Median Tectonic Line; I-STL, Itoigawa-Shizuoka Tectonic Line.

Fig. 2. Route map and sample localities of the Niihama area, showing lithology and mesoscopic structures (orientations of foliation, D_3 fold axis, fault and quartz slickenfibre). See Fig. 1b for location. Traces of lithological key beds are shown by dashed lines. Modified after El-Fakharani and Takeshita (2008). See the literature for definitions of domains A and B, and detailed D_3 fold and fault structures in domain A of Kokuryo river.

Fig. 3. Photographs of outcrop-scale D_2 normal faults, Niihama area, southwest Japan. (a) Note a normal displacement and dragging of the quartz veins parallel to the D_1 foliation. The fault plane strikes N85^{o}E and dips north at 44^{o}. (b) Quartz slickenfibre on fault plane showing a top-to-the-NNW sense of shear (shown by an arrow). The fault plane strikes N7^{o}E and dips east at 33^{o}, and the quartz slickenfibre trends S19^{o}E and plunges SSE at 16^{o}, apparently showing the

reverse sense of shear inferred from the step in the quartz slickenfibre. The localities of the outcrops are shown in Figure 2.

Fig. 4. (a) A microphotograph of a lens domain consisting of mostly recrystallized quartz grains and a small amount of phengite mica in quartz schist (Nishi-3-R) showing image under crossed polarizers with λ-plate inserted and (b) trace of recrystallized quartz and mica grain boundaries drawn with the Adobe Photoshop software. Mica grains were shown in black.

Fig. 5. A schematic diagram showing a new method to determine the degree of grain boundary undulation. See text for explanations. The number for the equation corresponds to that in text.

Fig. 6. Microstructures in quartz schist samples deformed at D_2 phase. (a) Kink bands (denoted by dashed lines) and lobate recrystallized grain boundaries (indicated by small arrows) of quartz from sample Nishi-1. Microstructures formed at D_1 phase are mostly preserved in this domain. (b) Shear bands in sample Nishi-1. Note alignment of phengite mica along a few arrayed shear bands and a micro-shear zone consisting of very-fine-grained quartz aggregates along a major one (shown by dashed lines with the sense indicated by arrows). (c) Maginification of part of Fig. 6b. See Fig. 6b for location. Note that very-fine-grained quartz originated as dynamically recrystallized grains at a tip of shear band, and very tiny aligned phengite mica is also grown between these grains in a dashed frame. (d) Micro-shear zone in sample Nishi-2 defined by very-fine-grained quartz aggregates and aligned phengite mica parallel to the shear zone boundary. (e) Microstructure consisting of the alternation of quartz lens and micro-shear zone (shown by dashed lines) in sample Nishi-2. Small arrows at quartz lens and micro-shear zone

interfaces indicate the dissolution front of quartz lens. Note that there are two sets of micro-shear zone: set A parallel to the original foliation and set B oblique to it (i.e. Riedel shear). A top-to-the-NW sense of shear (shown by arrows) is evident from dragging of the quartz lens (shown by dotted lines). (f) Micro-shear zone and irregularly shaped recrystallized quartz grains with many straight grain boundaries in sample Nishi-5. Note that many phengite mica grains were grown. (g) Maginification of part of Fig. 6f. See Fig. 6f for location. Note that straight grain boundaries were formed by grain growth of quartz pinned by phengite mica (shown by small arrows).

Fig. 7. Dislocation substructures observed with a TEM. (a) Sample Nishi-1. (b) Domain Nishi-2-S. Note that while dislocations are tangled and finally arranged to form sub-boundaries such as dislocation network (N) in (a), they are not tangled in (b). Also, dislocation loop (L) is common in (a).

Fig. 8. Equal-area and lower-hemisphere projections of quartz *c*-axis orientations from selective domains of quartz schist samples. (a) Domains with a strong type-I crossed girdle quartz *c*-axis fabric ($FI \geq 0.45$). (b) Domains with a weak type-I crossed girdle quartz *c*-axis fabric ($0.2 \leq FI < 0.45$). (c) Domains with a random quartz *c*-axis fabric ($FI < 0.2$). Domain names are shown at the top of each diagram, and fabric intensity (*FI*) and number of measurements (N) are indicated at lower left and right corners of each diagram, respectively. Schematic figure showing the fabric skeleton of asymmetrical type I crossed girdle quartz *c*-axis fabric with leading and trailing edges after Law (1987) is drawn at an upper left corner of Fig. 8a.

Fig. 9. Diagram showing average normalized perimeter ($\overline{P_{nor}}$) versus fabric intensity (*FI*) from all the subdomains. Fabric intensities in all the subdomains in each domain and domains Nishi-5-A, B are assumed to be the same. Regression line and square of correlation coefficient (C^2) are also shown with the slope and *y*-intercept.

Fig. 10. *R* (aspect ratio) versus ϕ (orientation of long axis with respect to the foliation orientation) diagram of recrystallized quartz grains in *XZ*-section for all the domains from analyzed quartz schist samples. (a) Domains with a strong quartz *c*-axis fabric ($FI \geq 0.45$). (b) Domains with a weak quartz *c*-axis fabric ($0.2 \leq FI < 0.45$). (c) Domains with a random quartz *c*-axis fabric ($FI < 0.2$). Schematic figure showing the ellipse fit of a recrystallized quartz grain is drawn at an upper left corner of Fig. 10a.

Fig. 11. (a) Diagram showing average normalized perimeter ($\overline{P_{nor}}$) versus area fraction of mica (*MF*) from all the subdomains, and (b) fabric intensity (*FI*) versus area fraction of mica (*MF*) from all the domains in analyzed quartz schist samples. Area fraction of mica (*MF*) in all the subdomains in each domain is assumed to be the same for Figs. 11a. For all the correlation diagrams, regression line and square of correlation coefficient (C^2) are also shown with the slope and *y*-intercept.

Fig. 12. Schematic diagram showing the model of coupled micro-faulting and pressure solution creep after Bos and Spiers (2002). Element A and B represent frictional sliding along mica, and pressure solution in quartz, respectively. μ, η, σ_n and σ are coefficient of internal friction, viscosity, normal stress and differential stress, respectively.

Fig. 13. Schematic diagram showing the microstructural development and associated deformation mechanisms with increasing shear strain in the analyzed quartz schist. See text for explanations.

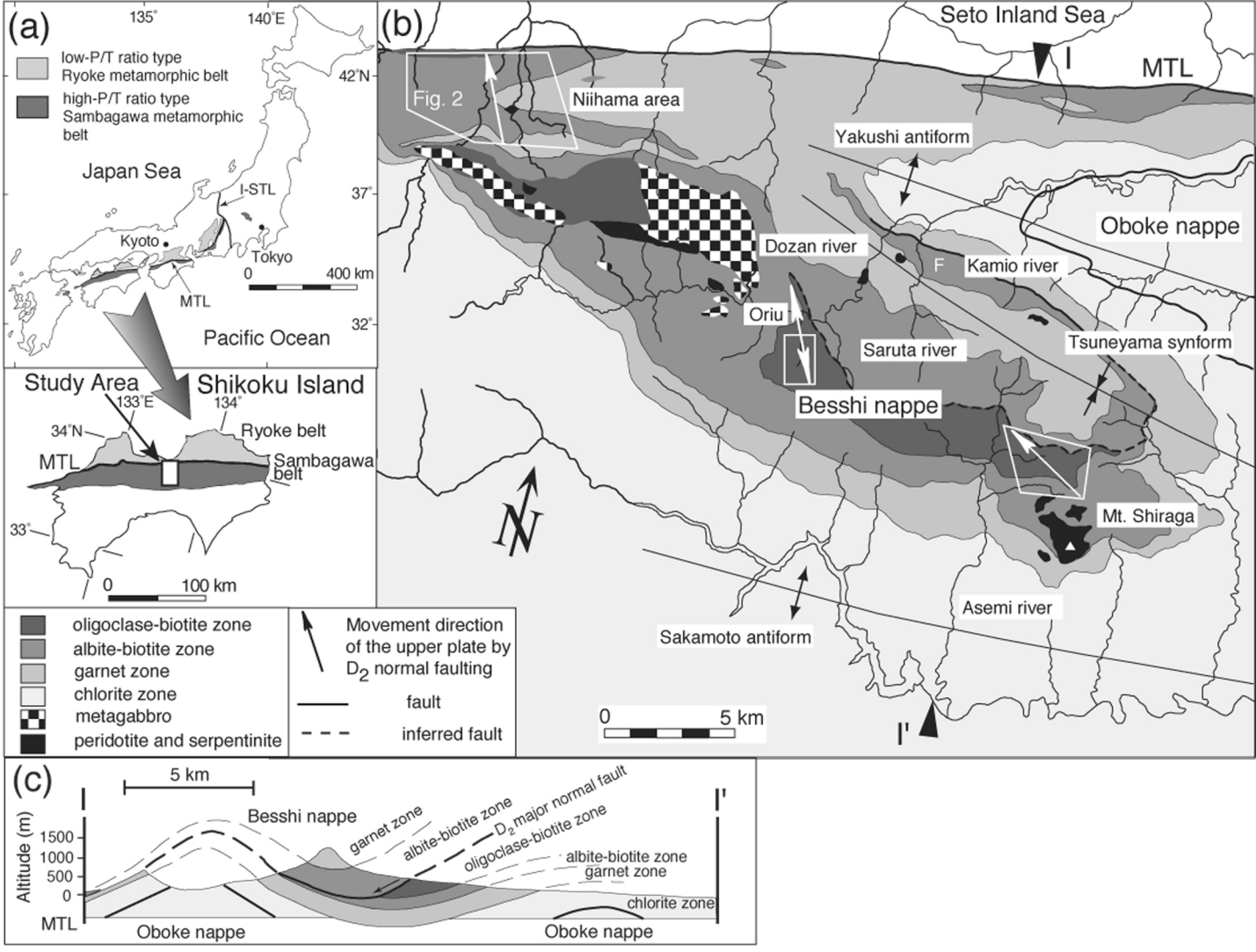
(a)
135°
140°E
42°N
37°
32°
low-P/T ratio type
Ryoke metamorphic belt
high-P/T ratio type
Sambagawa metamorphic belt
Japan Sea
I-STL
Kyoto
Tokyo
0
400 km
MTL
Pacific Ocean
Study Area
Shikoku Island
133°E
134°
34°N
Ryoke belt
MTL
Sambagawa belt
33°
0
100 km
(b)
Seto Inland Sea
I
MTL
Fig. 2
Niihama area
Yakushi antiform
Oboke nappe
Dozan river
F
Kamio river
Oriu
Saruta river
Tsuneyama synform
Besshi nappe
Mt. Shiraga
N
Asemi river
Sakamoto antiform
0
5 km
I'
oligoclase-biotite zone
albite-biotite zone
garnet zone
chlorite zone
metagabbro
peridotite and serpentinite
Movement direction of the upper plate by D2 normal faulting
fault
inferred fault
(c)
5 km
I
I'
Besshi nappe
garnet zone
albite-biotite zone
D2 major normal fault
oligoclase-biotite zone
albite-biotite zone
garnet zone
chlorite zone
Altitude (m)
1500
1000
500
0
MTL
Oboke nappe
Oboke nappe

Fig. 1

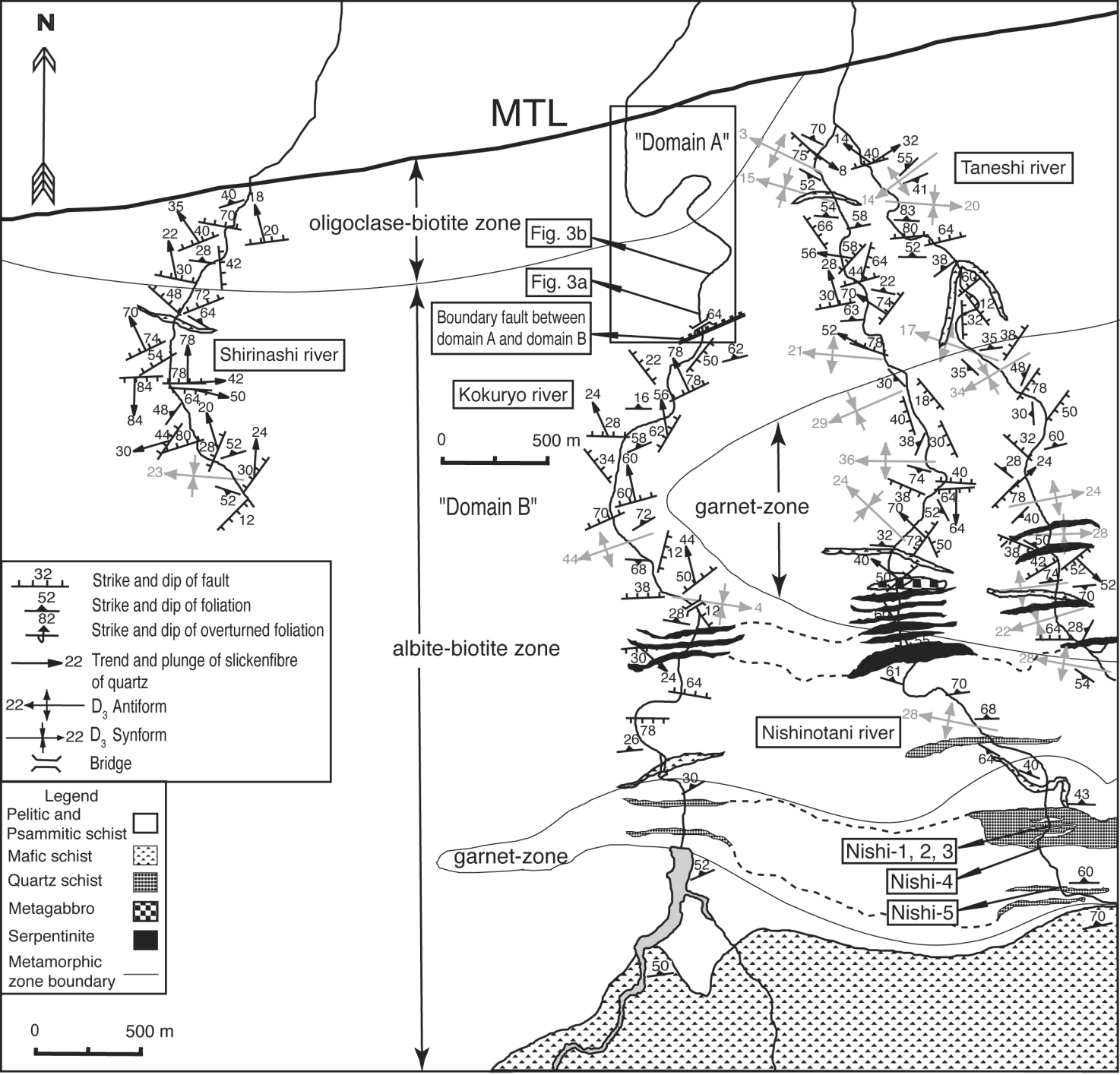
N
MTL
"Domain A"
Taneshi river
oligoclase-biotite zone
Fig. 3b
Fig. 3a
Boundary fault between domain A and domain B
Shirinashi river
Kokuryo river
0
500 m
"Domain B"
garnet-zone
albite-biotite zone
Nishinotani river
garnet-zone
Nishi-1, 2, 3
Nishi-4
Nishi-5
Strike and dip of fault
Strike and dip of foliation
Strike and dip of overturned foliation
Trend and plunge of slickenfibre of quartz
D3 Antiform
D3 Synform
Bridge
Legend
Pelitic and Psammitic schist
Mafic schist
Quartz schist
Metagabbro
Serpentinite
Metamorphic zone boundary
0
500 m

Fig. 2

Fig. 3

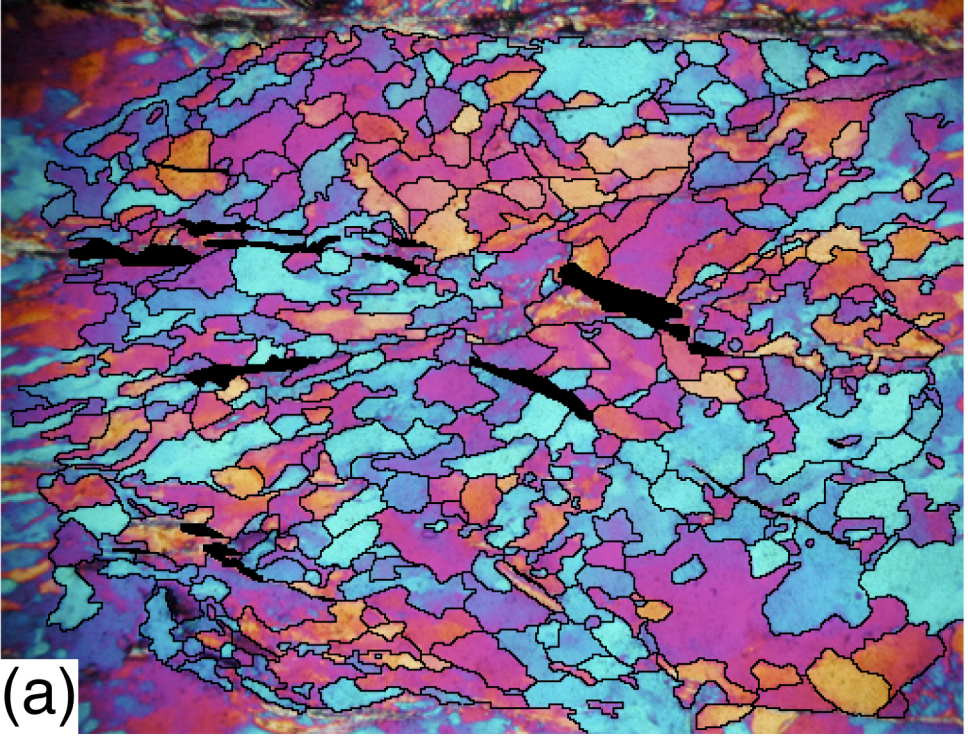

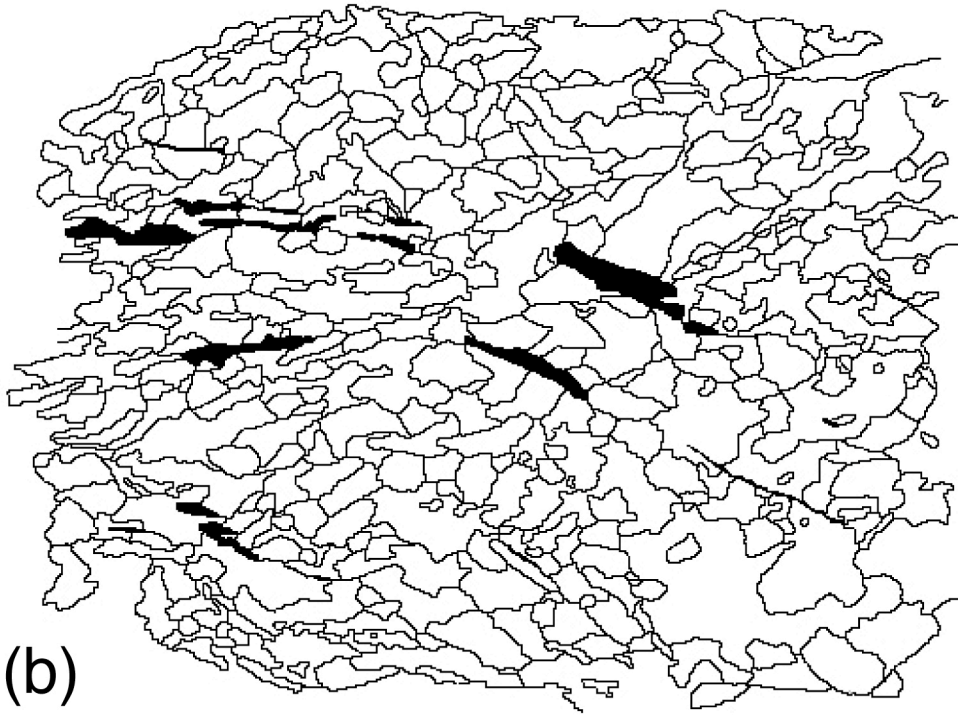

Fig. 4

New method to determine the degree of grain boundary undulation

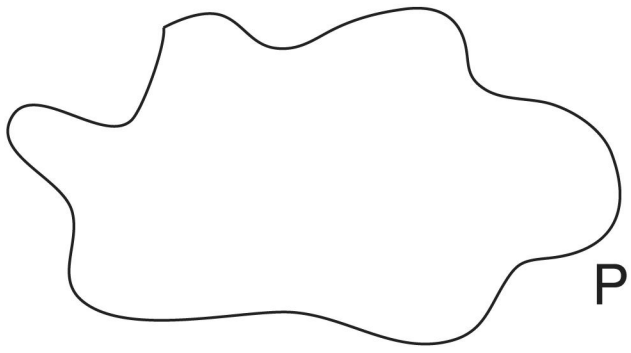

real shape

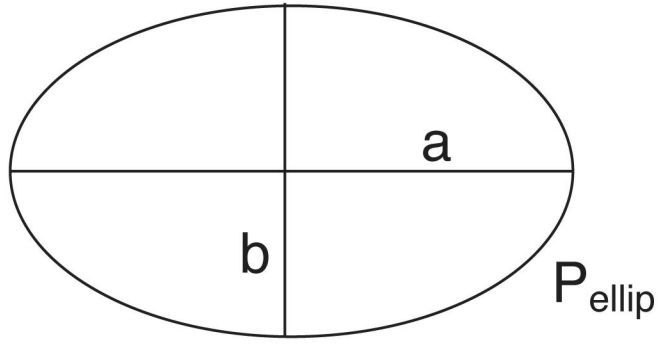

equivalent fitted ellipse

a and b: Length of long and short axes of the fitted ellipse

P: Perimeter of real ellipse

P_{ellip}: Perimeter of fitted ellipse

$$P_{ellip}=2*\pi*SQRT(((a/2)^2+(b/2)^2)/2) \quad (3)$$

The degree of grain boundary undulation=P/P_{ellip}

Fig. 5

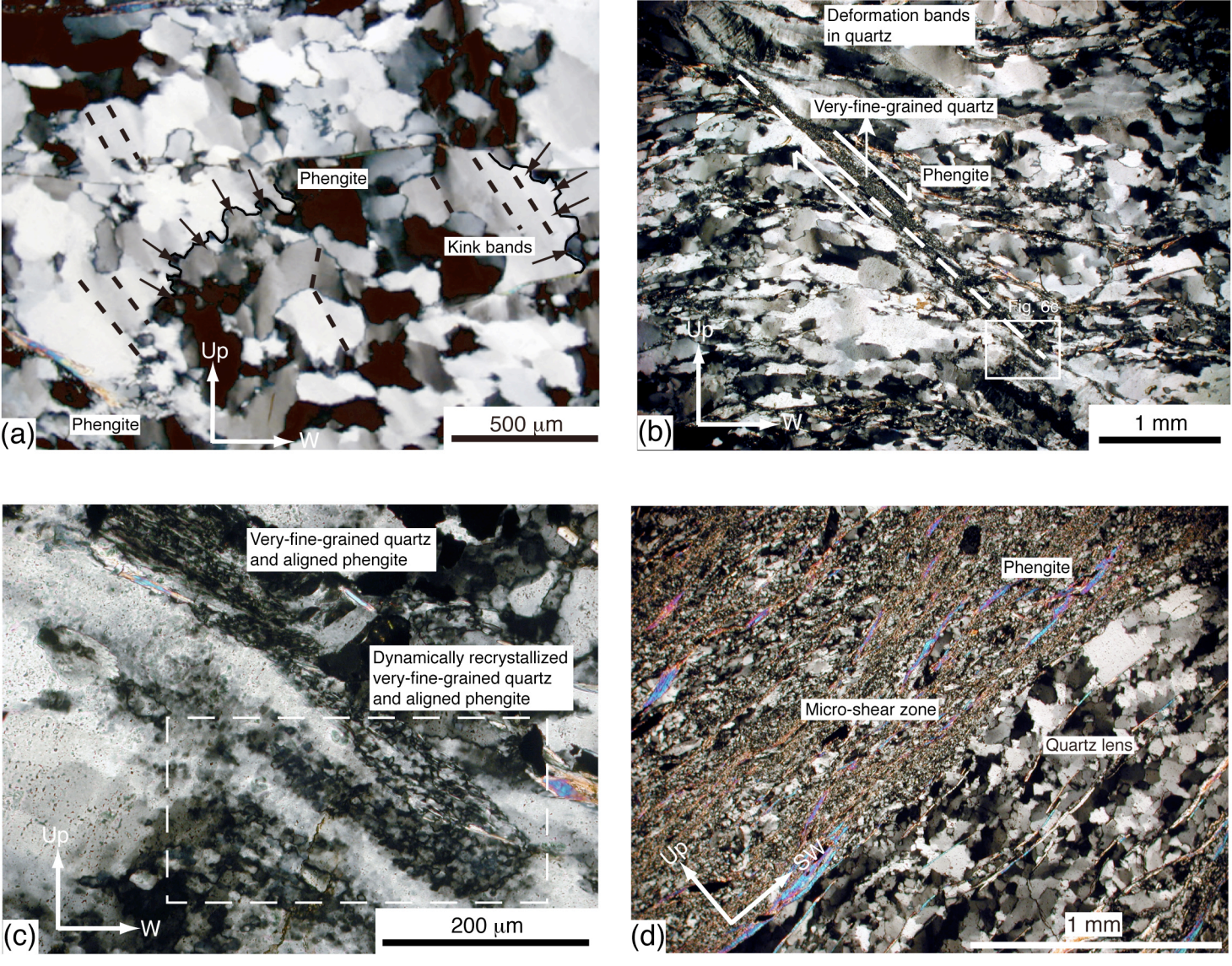
Phengite
Kink bands
Up
W
(a)
Phengite
500 μm
Deformation bands
in quartz
Very-fine-grained quartz
Phengite
Fig. 6c
Up
W
(b)
1 mm
Very-fine-grained quartz
and aligned phengite
Dynamically recrystallized
very-fine-grained quartz
and aligned phengite
Up
W
(c)
200 μm
Phengite
Micro-shear zone
Quartz lens
Up
SW
(d)
1 mm

Fig. 6

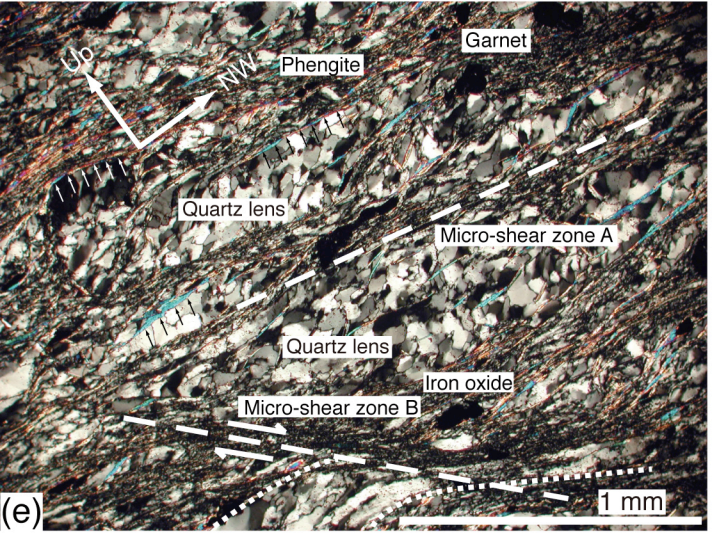

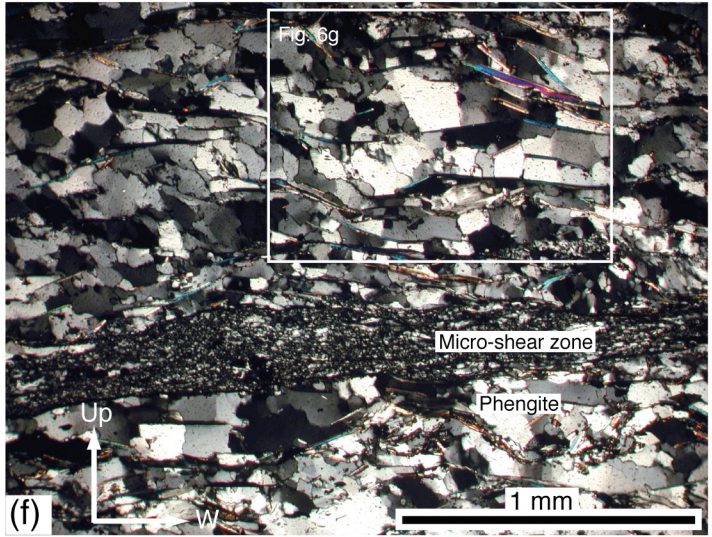

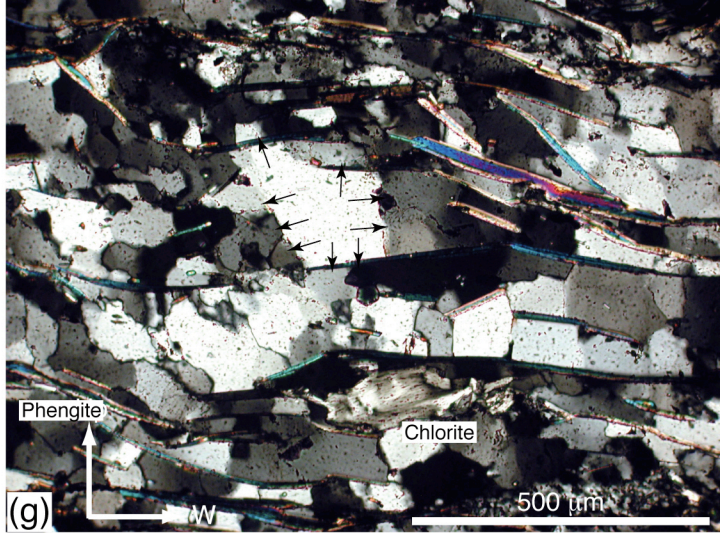

Fig. 6 continues

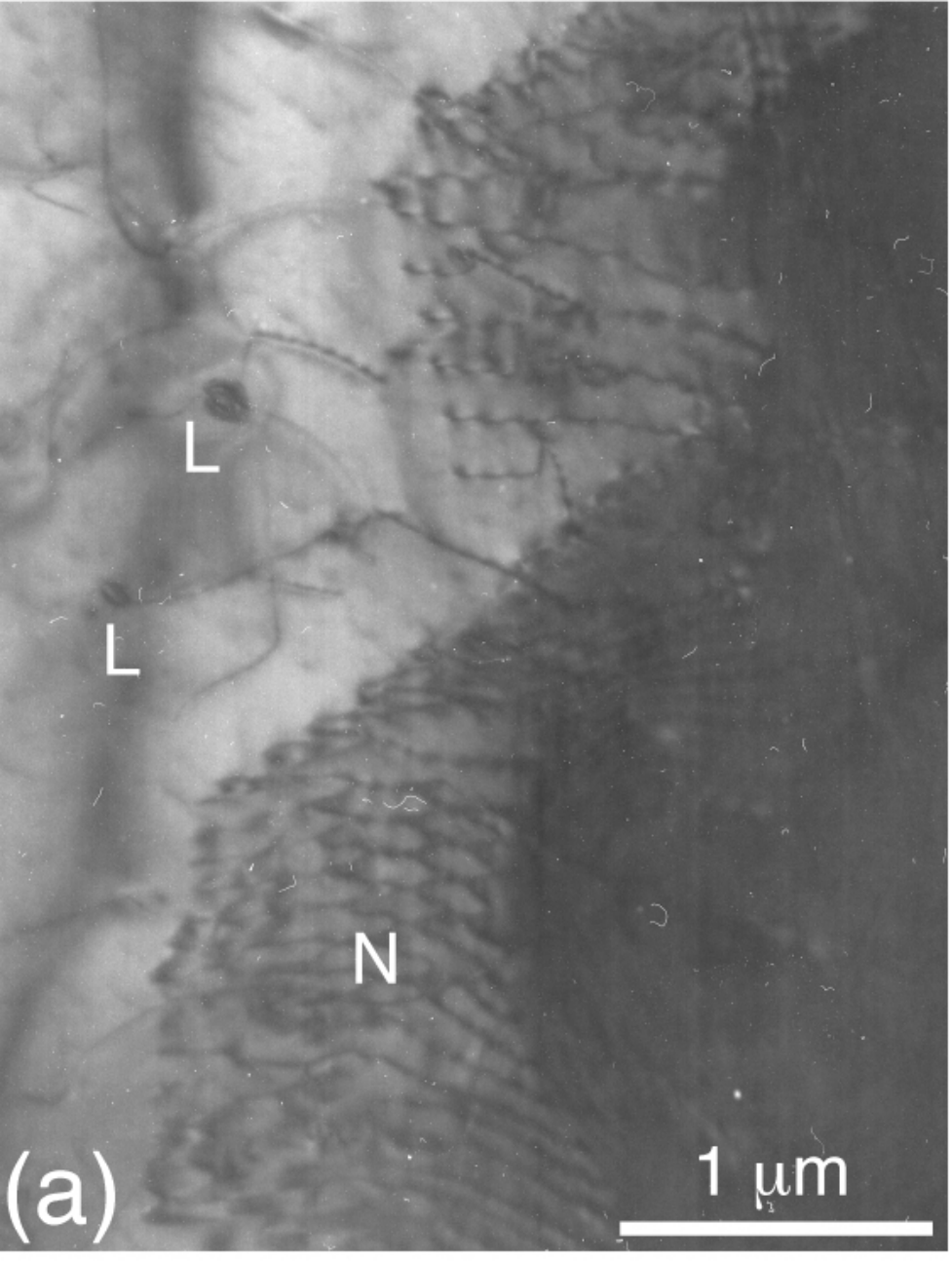

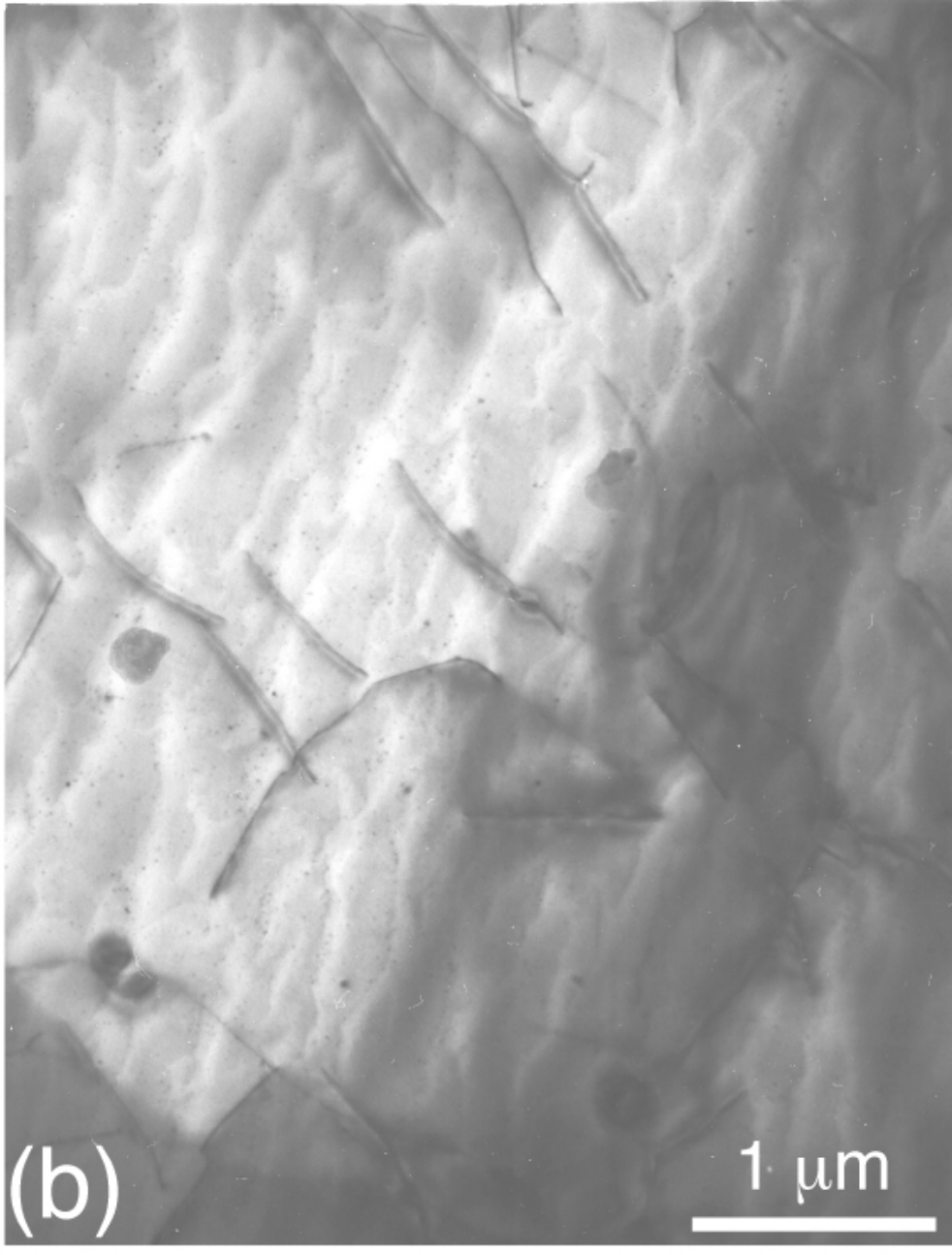

Fig. 7

(a) Strong quartz *c*-axis fabric (FI≥0.45)

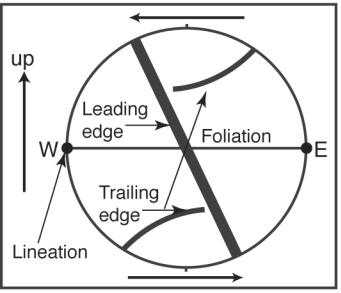

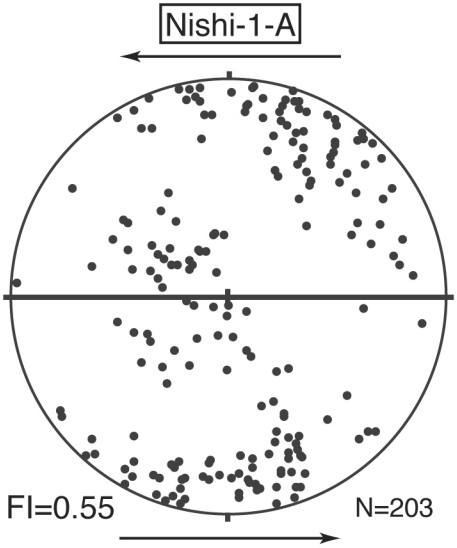

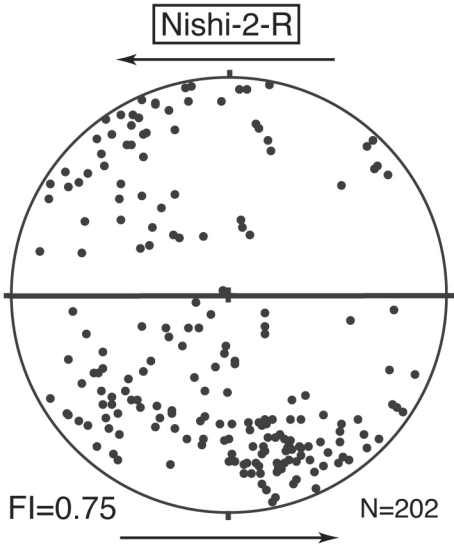

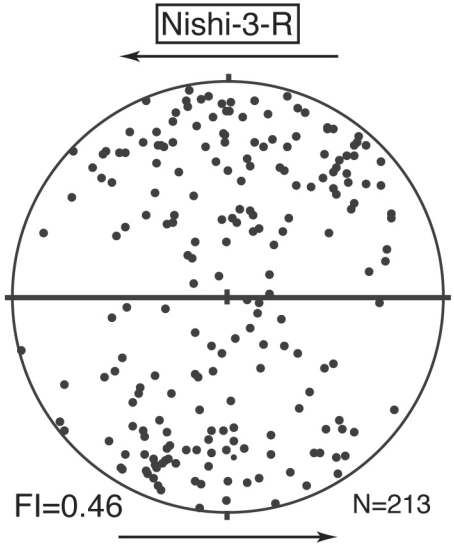

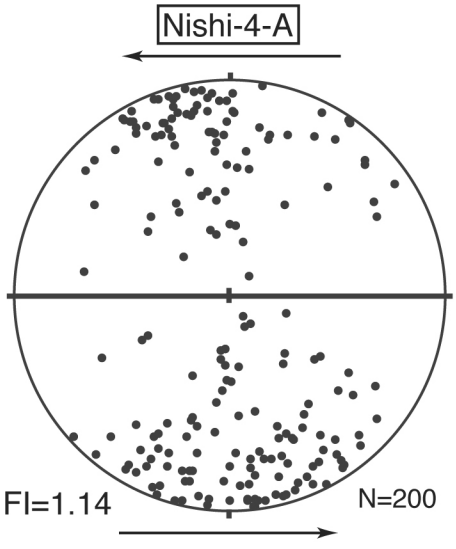

Fig. 8a

(b) Weak quartz *c*-axis fabric (0.2≤FI<0.45)

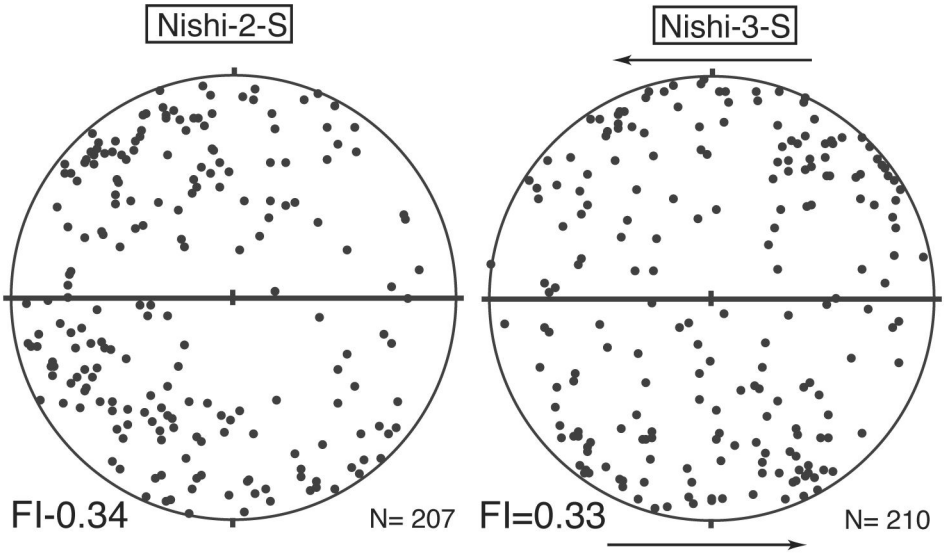

(c) Random quartz *c*-axis fabric (FI<0.2)

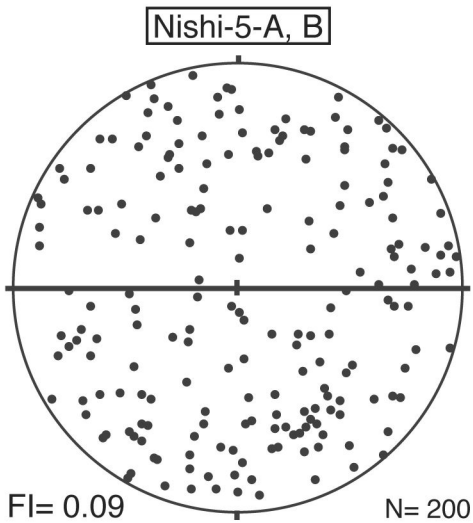

Figs. 8b, c

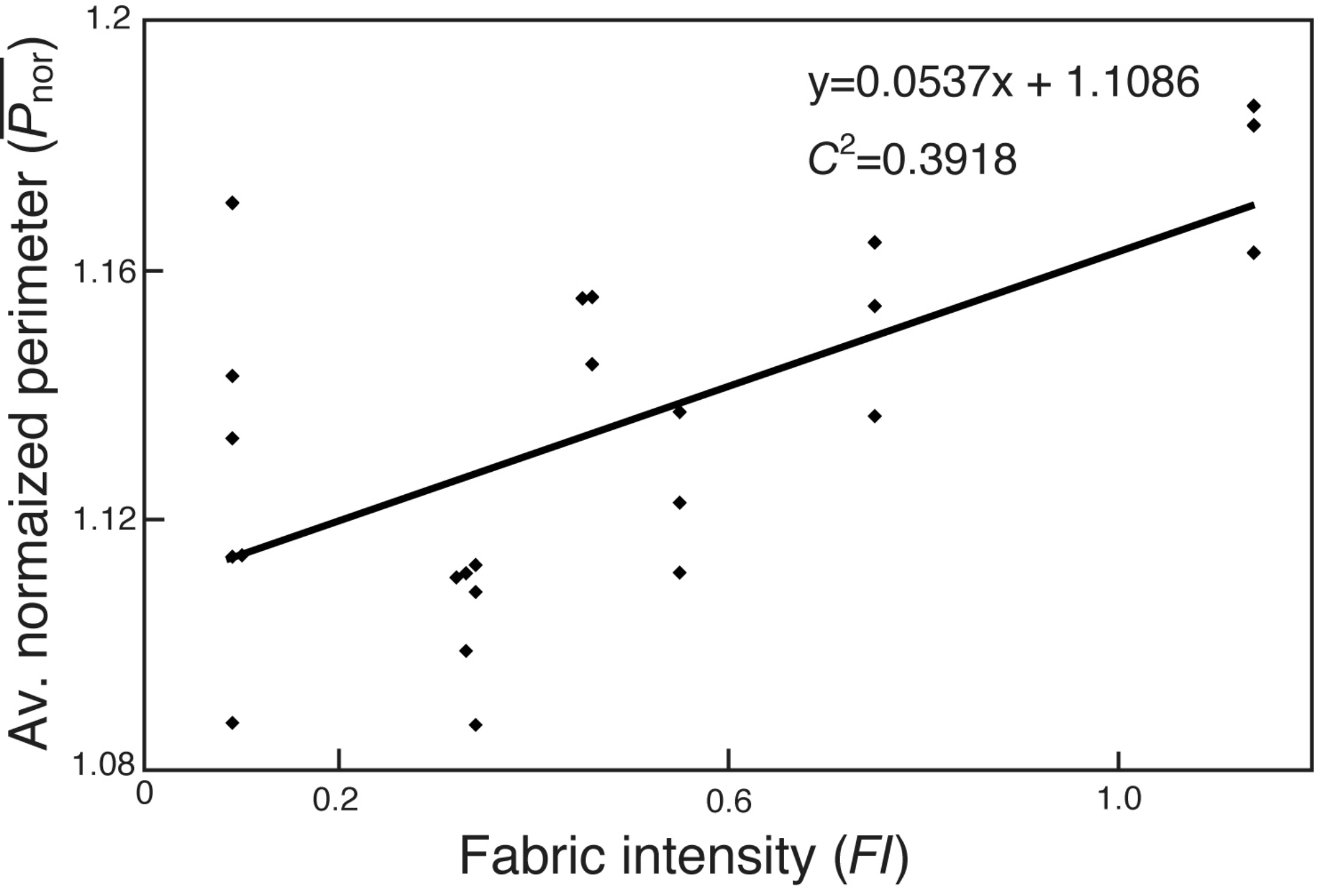
y=0.0537x + 1.1086
C^2=0.3918
Av. normaized perimeter ($\overline{P_{nor}}$)
Fabric intensity (*FI*)
1.2
1.16
1.12
1.08
0
0.2
0.6
1.0

Fig. 9

(a) Strong *c*-axis fabric (FI≥0.45)

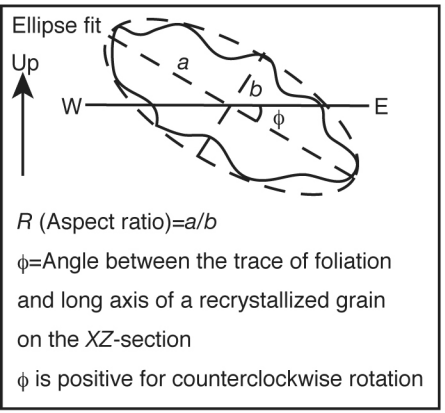

R (Aspect ratio)=*a*/*b*

ϕ=Angle between the trace of foliation and long axis of a recrystallized grain on the *XZ*-section

ϕ is positive for counterclockwise rotation

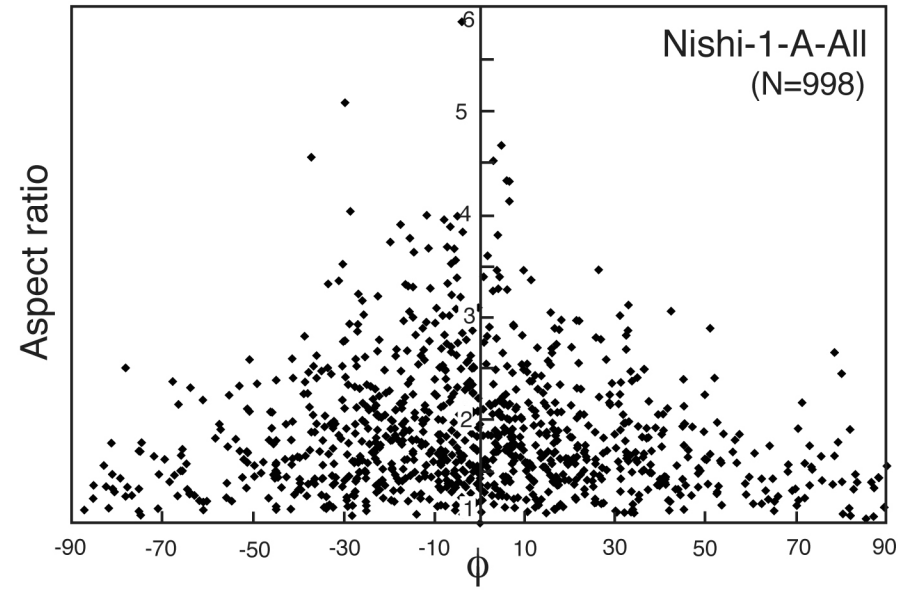

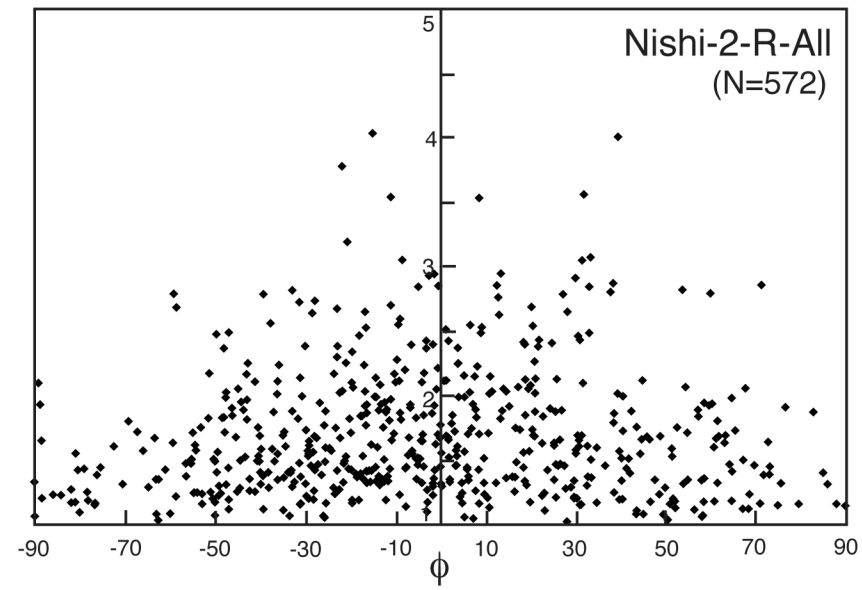

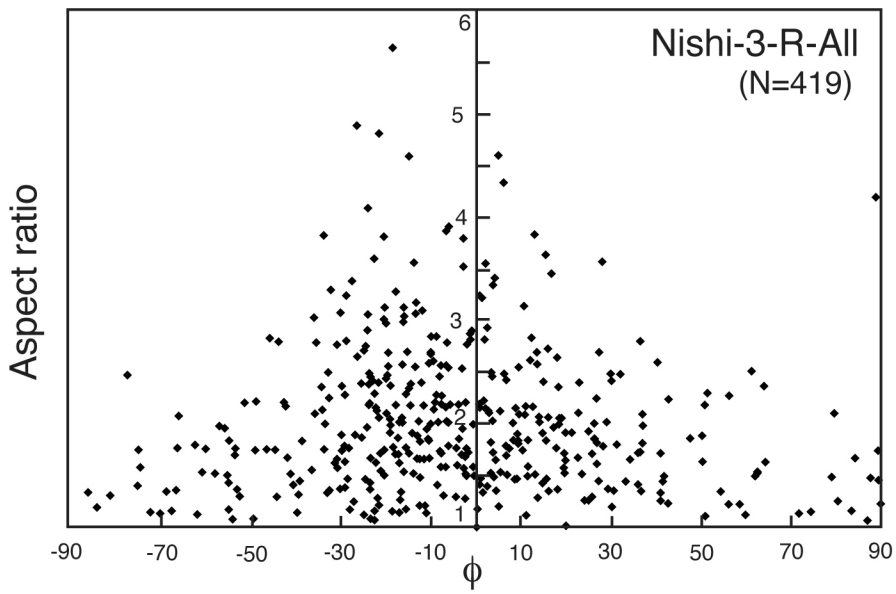

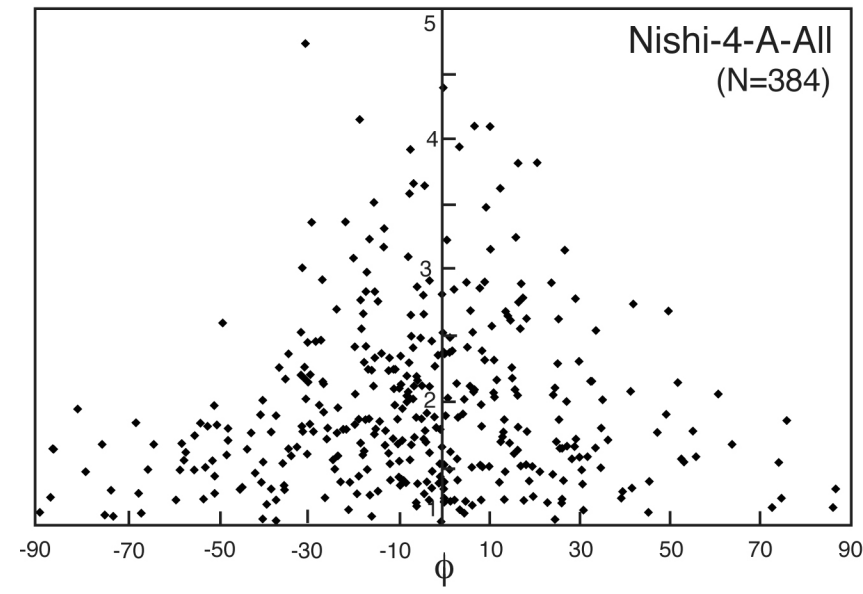

Fig. 10a

(b) Weak *c*-axis fabric (0.2≤FI<0.45)

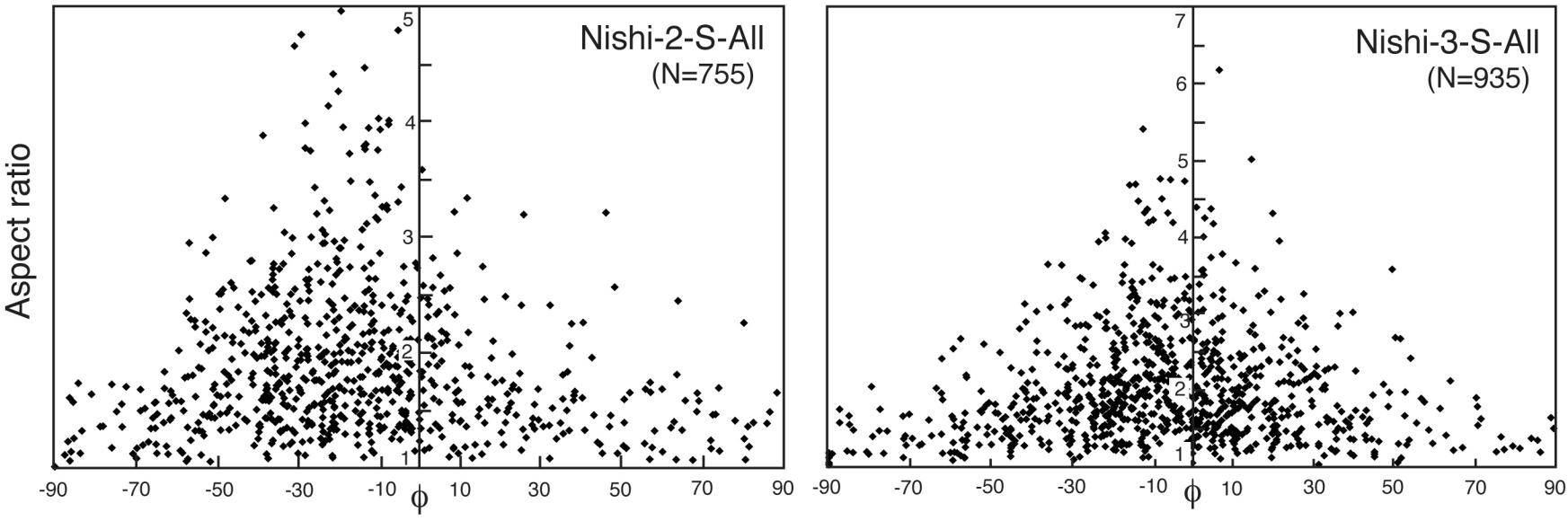

(c) Random *c*-axis fabric (FI<0.2)

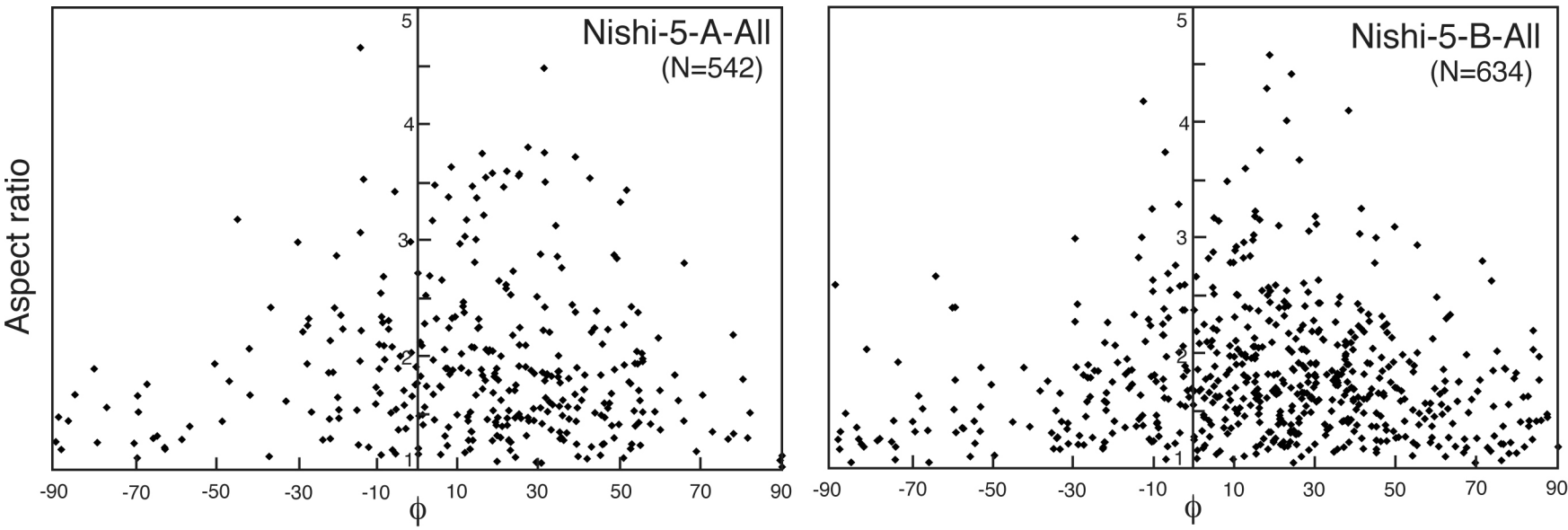

Figs. 10b, c

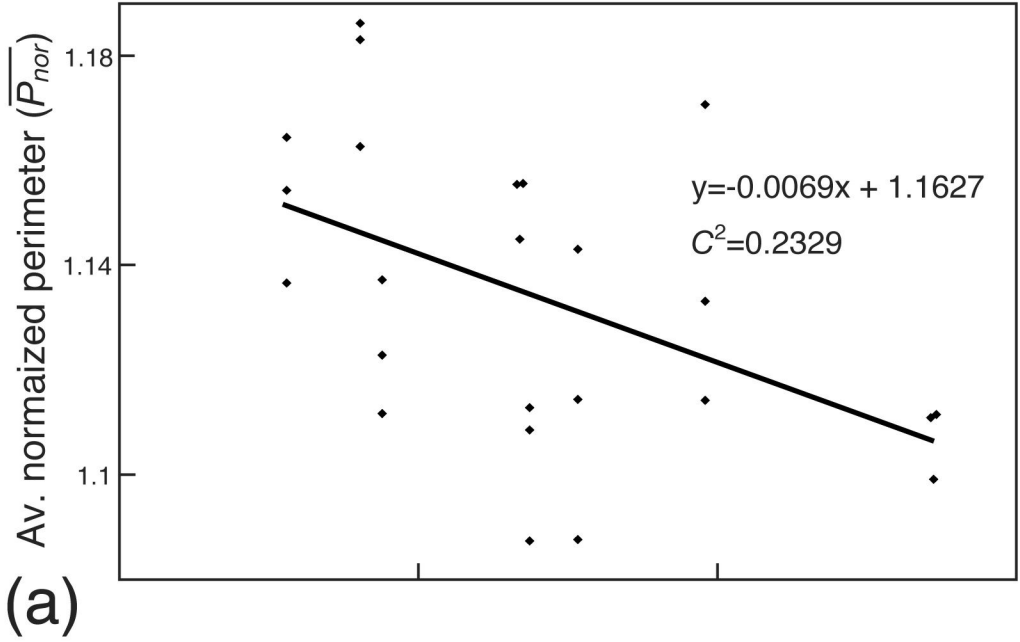
Av. normaized perimeter ($\overline{P_{nor}}$)
1.18
1.14
1.1
y=-0.0069x + 1.1627
C^2=0.2329

(a)

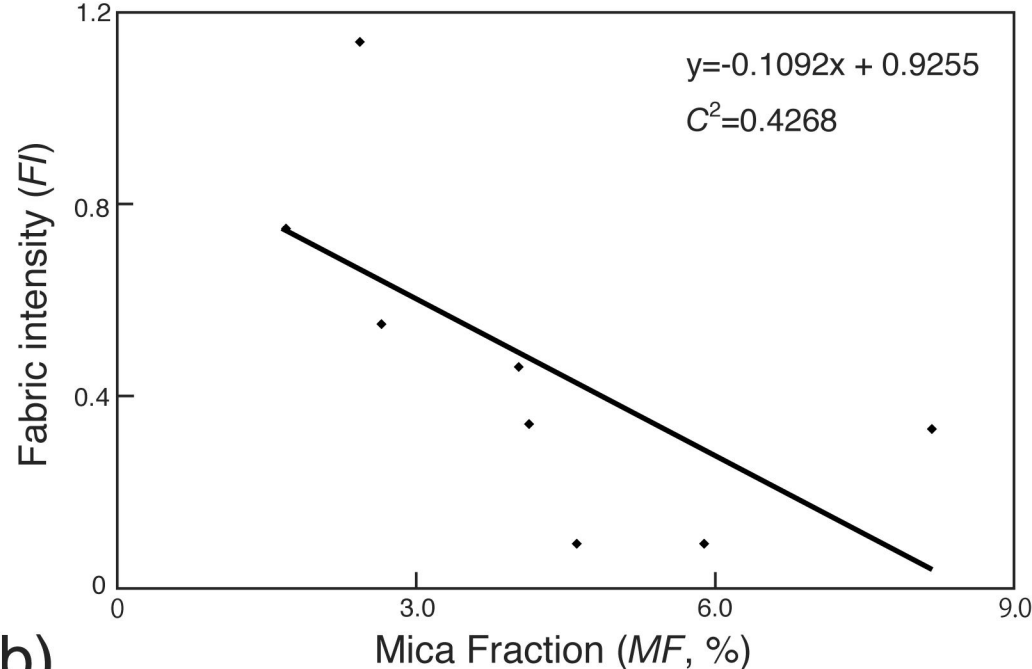
Fabric intensity (*FI*)
1.2
0.8
0.4
0
y=-0.1092x + 0.9255
C^2=0.4268
0
3.0
6.0
9.0
Mica Fraction (*MF*, %)

(b)

Fig. 11a, b

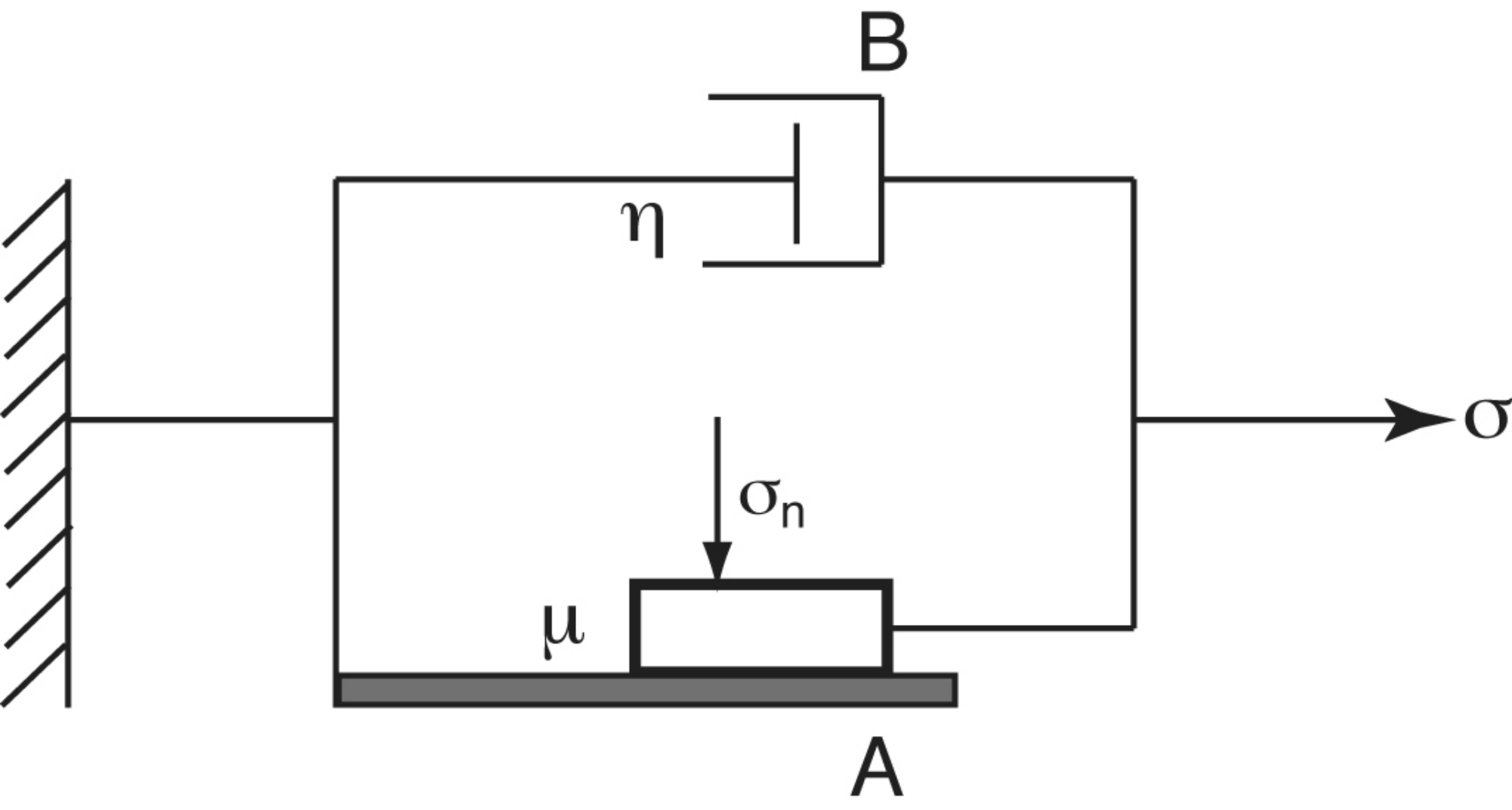

Fig. 12

Stage 1

Formation of shear bands and micro-shear zones are dominant. D_1 microstructures are preserved in quartz lenses (e.g. Nishi-1, Nishi 4).

Stage 3

No shear bands are newly formed in quartz lenses, the constituent quartz grains of which are all precipitated from the solution, indicating that they are deformed by pressure solution alone (e.g. Nishi-5).

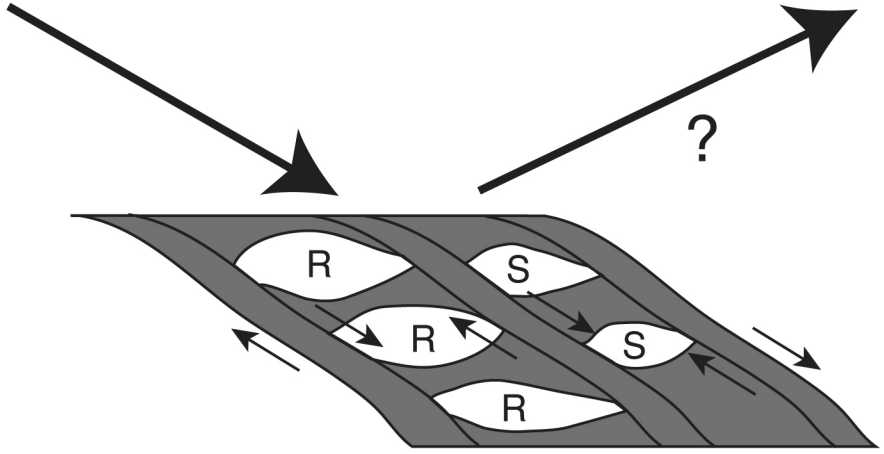

Quarz lens

Shear bands and Micro-shear zone

Sense of shear

Stage 2

The volume fraction of micro-shear zones increases. Although D_1 microstructures are essentially preserved and the formation of shear bands is dominant in less sheared quartz lenses (Rs), pressure solution creep becomes dominated in more sheared quartz lenses (Ss) (e.g. Nishi-2, Nishi-3).

Fig. 13

Table 1. Summary of the image analyses for recrystallized quartz and mica grains and quartz *c*-axis fabric measurements in the quartz schist samples. See a supplementary material for *n and* C^2.

Sample, domain and subdomain name	N	$\overline{D_{eq}}$ (μm)	$\bar{P}$ (μm)	$\bar{R}$	$\overline{P_{eq}}$ (μm)	$\overline{P_{nor}}$	*n*	C^2	*FI*	*MF* (%)
Nishi-1-A-1	319	82.2	330.4	1.91	290.5	1.137	1.2201	0.9697	0.55	2.63
Nishi-1-A-2	384	73.9	286.6	1.85	257.8	1.112	1.2088	0.9732	0.55	2.63
Nishi-1-A-3	295	79.5	311.6	1.87	277.5	1.123	1.1886	0.9711	0.55	2.63
Nishi-2-R-1	186	51.7	201.2	1.76	177	1.137	1.1606	0.9681	0.75	1.67
Nishi-2-R-2	198	57	222.8	1.65	193	1.154	1.1757	0.9825	0.75	1.67
Nishi-2-R-3	188	56	222.9	1.71	191.4	1.165	1.1204	0.9776	0.75	1.67
Nishi-2-S-1	254	55.9	216.9	1.87	194.9	1.113	1.154	0.9731	0.34	4.11
Nishi-2-S-2	201	55.8	221.6	1.98	199.9	1.109	1.1984	0.9755	0.34	4.11
Nishi-2-S-3	300	52.5	200.4	1.89	184.3	1.087	1.1725	0.9656	0.34	4.11
Nishi-3-R-1	131	59.2	243.4	1.77	210.6	1.156	1.1887	0.9666	0.46	4.01
Nishi-3-R-2	127	55	229.7	2.15	200.6	1.145	1.2149	0.9569	0.46	4.01
Nishi-3-R-3	161	60.5	249.6	1.95	216	1.156	1.1599	0.9717	0.46	4.01
Nishi-3-S-1	357	40.2	161.4	2.05	145.2	1.112	1.2246	0.973	0.33	8.16
Nishi-3-S-2	271	37.5	150.8	2.05	137.2	1.099	1.2532	0.9704	0.33	8.16
Nishi-3-S-3	307	42	165.3	1.9	148.8	1.111	1.1986	0.9763	0.33	8.16
Nishi-4-A-1	154	75.7	317.6	1.89	268.4	1.183	1.2707	0.9726	1.14	2.41
Nishi-4-A-2	127	78.4	329.9	2.04	283.7	1.163	1.2429	0.9612	1.14	2.41
Nishi-4-A-3	103	91.8	379.3	1.84	319.7	1.186	1.1928	0.9883	1.14	2.41
Nishi-5-A-1	170	55.8	221.1	1.94	198.4	1.114	1.1982	0.9756	0.09	4.59
Nishi-5-A-2	144	52.2	199.8	1.9	183.7	1.088	1.1658	0.9756	0.09	4.59
Nishi-5-A-3	228	60.6	242.7	1.87	212.3	1.143	1.1913	0.9804	0.09	4.59
Nishi-5-B-1	195	53.2	203.9	1.76	183	1.114	1.1711	0.9853	0.09	5.87
Nishi-5-B-2	243	55.3	216.9	1.81	191.4	1.133	1.2055	0.9772	0.09	5.87
Nishi-5-B-3	196	57.2	233.7	1.82	199.6	1.171	1.2339	0.9756	0.09	5.87

N, number of analyzed quartz grains; $\overline{D_{eq}}$, average equivalent diameter; $\bar{P}$, average perimeter; $\bar{R}$, average aspect ratio; $\overline{P_{eq}}$, average equivalent perimeter; $\overline{P_{nor}}$, average normalized perimeter; *n*, fractal dimension of grain shape; C^2, square of correlation coefficient for *n*; *FI*, fabric intensity; *MF*, mica area fraction.

Table 2. Square of correlation constant (C^2) and *T*-value for correlation between two different microstructural indices for the quartz schist samples. See captions of Table 1 for abbreviations of different microstructural indices. See text for explanation of the *T*-value.

Correlation between two different microstrauctural indices	C^2	*T*-value
$\overline{P_{nor}}$ versus *FI*	0.3918	3.764
$\overline{P_{nor}}$ versus *MF*	0.2329	2.583
FI versus *MF*	0.4268	4.048